Monthly Notices of the ROYAL ASTRONOMICAL SOCIETY
MNRAS 529, 296–319 (2024) https://doi.org/10.1093/mnras/stae424
Advance Access publication 2024 February 10

Double-mode RR Lyrae stars observed by *K2*: analysis of high-precision *Kepler* photometry

James M. Nemec,[1★] Amanda F. Linnell Nemec,[1] Pawel Moskalik,[2★] László Molnár,[3,4,5] Emese Plachy,[3,4,5] Róbert Szabó[3,4,5] and Katrien Kolenberg[6,7]

[1] International Statistics and Research Corporation, , PO Box 39, Brentwood Bay, V8M1R3 British Columbia, Canada
[2] Nicolaus Copernicus Astronomical Center, 00-716 Warszawa, Poland
[3] Konkoly Observatory, HUN-REN CSFK, Konkoly-Thege Miklós út 15-17, H-1121 Budapest, Hungary
[4] CSFK, MTA Centre of Excellence, Budapest, Konkoly-Thege Miklós út 15-17, H-1121 Budapest, Hungary
[5] ELTE Eötvös Loránd University, Institute of Physics and Astronomy, Pázmány Pétersétány 1/A, H-1117 Budapest, Hungary
[6] Institute of Astronomy, 3001 KU Leuven, Belgium
[7] Physics Department, University of Antwerp, 2020 Antwerpen, Belgium

Accepted 2024 February 6. Received 2024 February 6; in original form 2023 December 12

ABSTRACT

The results of a Fourier analysis of high-precision *Kepler* photometry of 75 double-mode RR Lyrae (RRd) stars observed during NASA's *K2* Mission (2014-18) are presented. Seventy-two of the stars are 'classical' RRd (cRRd) stars lying along a well-defined curve in the Petersen diagram and showing no evidence of Blazhko modulations. The remaining three stars are 'anomalous' RRd (aRRd) stars that lie well below the cRRd curve in the Petersen diagram. These stars have larger fundamental-mode amplitudes than first-overtone amplitudes and exhibit Blazhko variations. Period-amplitude relations for the individual pulsation components of the cRRd stars are examined, as well as correlations involving Fourier phase-difference and amplitude-ratio parameters that characterize the light curves for the two radial modes. A simple statistical model relating the fundamental (P_0) and first-overtone (P_1) periods to [Fe/H] provides insight into the functional form of the Petersen diagram. A calibration equation for estimating $\mathrm{[Fe/H]_{phot}}$ abundances of 'classical' RRd stars is derived by inverting the model and using 211 field and 57 globular cluster cRRd stars with spectroscopic metallicities to estimate the model coefficients. The equation is used to obtain $\mathrm{[Fe/H]_{phot}}$ for the full sample of 72 *K2* cRRd stars and for 2130 cRRd stars observed by the ESA *Gaia* Mission. Of the 49 *K2* cRRd stars that are in the *Gaia* DR3 catalogue only five were found to be correctly classified, the remainder having been misclassified 'RRc' or 'RRab'.

Key words: methods: statistical – stars: abundances – stars: horizontal branch – stars: Population II – stars: variables: RR Lyrae – Galaxy: halo.

1 INTRODUCTION

Double-mode RR Lyrae (RRd) stars are old low-mass stars burning helium in their cores and pulsating simultaneously in the fundamental and first-overtone *radial* modes. As the two modes go in and out of phase the observed amplitude of the pulsation varies from cycle to cycle. In Hertzsprung–Russell diagrams RRd stars are found in the instability strip between the cooler RRab stars and the hotter RRc stars, and have effective temperatures $6200 < T_{\mathrm{eff}} < 7000$ K, luminosities $20 < \mathrm{L/L_{\odot}} < 60$, and masses $0.55 < \mathrm{M/M_{\odot}} < 0.90$ (Christy 1966; Cox, King & Hodson 1980; Cox, Hodson & Clancy 1983; Simon & Cox 1991; Kovács & Karamiqucham 2021; Netzel & Smolec 2022).

The first RR Lyrae star in which double-mode pulsation was observed was the high galactic latitude star AQ Leo (Jerzykiewicz & Wenzel 1977; see also Gruberbauer et al. 2007). The subsequent discovery of dozens of RRd stars in several globular clusters and dwarf galaxies led to a much-improved understanding of their properties. For instance, most RRd stars are now known to lie along a well-defined curve in a Petersen (1973) diagram (see Fig. 1), with the radial first-overtone pulsation mode usually dominating over the fundamental mode (see Fig. 2). Such stars will hereafter be referred to as 'classical' RRd (cRRd) stars. The RRd stars that lie off the 'Petersen curve', usually below but sometimes above, are commonly referred to as 'anomalous' RRd (aRRd) stars (Soszyński et al. 2016b). The aRRd stars tend to have larger fundamental than first-overtone amplitudes (blue open circles in Fig. 2) and often exhibit Blazhko variations. Both cRRd and aRRd stars exhibit the same approximately linear relationship between the two periods, with the aRRd stars showing more scatter than the cRRd stars (see fig. 15a of Nemec & Moskalik 2021, hereafter NM21).

It is now well-established from observations and pulsation models that the locations of cRRd stars in Petersen diagrams correlate with metal abundance and mass: the shorter the period the smaller the period ratio, the greater the metal abundance, and the smaller the mass. The period–metallicity correlation was first established

★ E-mail: jmn@isr.bc.ca, afln@isr.bc.ca (JMN); pam@camk.edu.pl (PM)

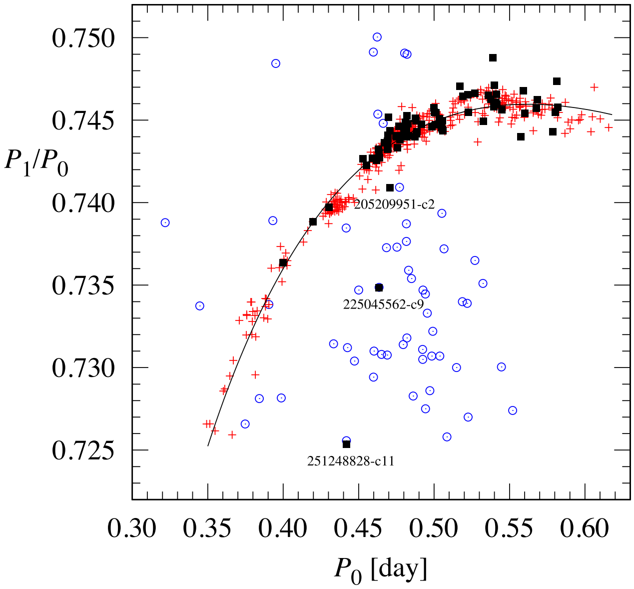

Figure 1. Petersen diagram for the 72 'classical' and three 'anomalous' RRd stars observed by *K2* (solid black squares). Also plotted are 458 Galactic Disc and Bulge cRRd stars (red plus signs) observed by OGLE (Soszyński et al. 2019) and 54 aRRd stars (blue circles). The aRRd stars are in the globular clusters M3 (4 stars; Jurcsik et al. 2015) and NGC 6362 (2 stars; Smolec et al. 2017a), in the Magellanic Clouds (20 in the LMC, two in the SMC; Soszyński et al. 2016b), and in the Galactic Bulge (28 stars; Soszyński et al. 2019). The equation of the fitted *K2* + OGLE curve is given in Section 4.4.2.

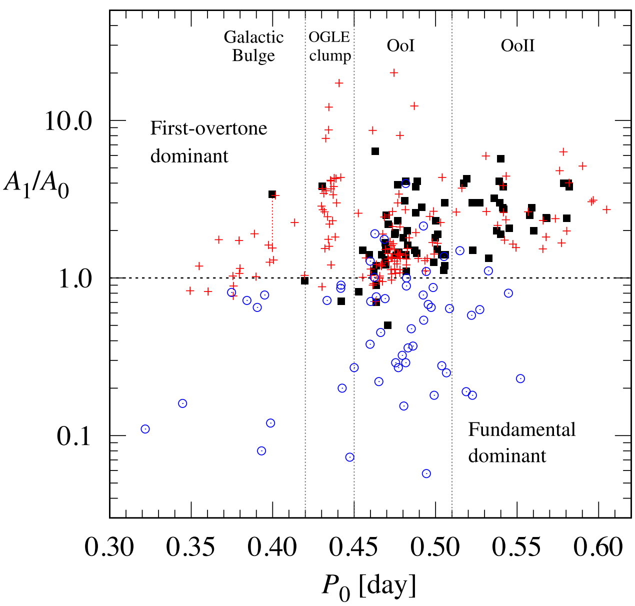

Figure 2. Amplitude-ratio diagram for the RRd stars observed by *K2* (same stars and same symbols as Fig. 1), where the fundamental and first-overtone amplitudes for the *K2* stars are Fourier first-term *Kp*-amplitudes and those for the OGLE stars are trough-to-peak (min-max) *I*-amplitudes. Three of the six *K2* stars with $A_1 < A_0$ are 'anomalous' RRd stars lying off the Petersen curve while the other three are 'classical' RRd stars. Graphs of A_1/A_0 versus period for RRd stars in the Large Magellanic Cloud previously were plotted by Alcock et al. (1997) and Soszyński et al. (2009).

when it was observed that the RRd stars in the most metal-poor globular clusters (i.e. Oosterhoff type II GCs), such as M15 (Sandage, Katem & Sandage 1981; Cox et al. 1983; Nemec 1985a) and M68 (Clement, Ferance & Simon 1993), have fundamental-mode periods P_0 greater than 0.51 d, while those in intermediate metallicity (Oo I) GCs, such as IC4499 (Clement et al. 1986; Walker & Nemec 1996) and M3 (Nemec & Clement 1989; Jurcsik et al. 2015, 2017) have shorter periods, $0.45 < P_0 < 0.51$ d. Many RRd stars have also been found in all the nearby dwarf galaxies (see Clementini et al. 2023, for references) and are being used to study the metallicity variations in those systems (see Braga et al. 2022) and their relationship to the history of our Galaxy. The discovery of large numbers of RRd stars in the Magellanic Clouds by the MACHO (Alcock et al. 1997, 2000, 2004) and OGLE (Soszyński et al. 2009, 2010, 2016a,b) surveys, and in the Bulge and Disc of our Galaxy (Soszyński et al. 2010, 2011, 2017a,b, 2019), extended the period-metallicity trend to shorter periods, revealing that most cRRd stars with periods P_0 between 0.42 and 0.45 d are located in a prominent clump of stars (Soszyński et al. 2014b; Kunder et al. 2019), and that the most metal-rich RRd stars (found mainly in the Galactic Bulge) have the shortest periods, with periods as short as $P_0 = 0.35$ d, period ratios as small as $P_1/P_0 = 0.725$, and metallicities as rich as [Fe/H]~ -0.35 dex (see Soszyński et al. 2011, 2014b).

Early theoretical models by Cox et al. (1980, 1983), which used Los Alamos opacities, hypothesized that the radial pulsation periods and their ratios are determined mainly by the mass M and metal abundance [Fe/H], and to a lesser degree by luminosity L and effective temperature $T_{\rm eff}$. Popielski, Dziembowski & Cassisi (2000, fig. 2) used stellar evolution and pulsation models with the newer opacities of Iglesias & Rogers (1991, 1996; see also Simon 1982; Seaton 1994) to illustrate the impact on location in the Petersen diagram of varying M, L, $T_{\rm eff}$, and [Fe/H]. Theoretical curves of constant mass and constant metallicity derived from such models are commonly overlaid onto the Petersen diagram as a means of inferring [Fe/H] and mass (see fig. 4 of Simon & Cox 1991, fig. 1 of Bono et al. 1996, fig. 1 of Alcock et al. 1997; fig. 3 of Kovács 2001; fig. 2 of Soszyński et al. 2014a; fig. 7 of Coppola et al. 2015; fig. 4 of Braga et al. 2022).

High-precision surveys from space, such as the MOST, CoRoT, *Kepler/K2*, *Gaia*, and *TESS* missions (see Molnár et al. 2022, for recent references), have led to the recognition that, in addition to radial pulsations, most, if not all, RRd stars exhibit low-amplitude *non-radial* pulsations (see Moskalik et al. 2018a,b). Such pulsations are present in all of the well-studied *K2* RRd stars, the most prominent having a period $P_{\rm nr} \sim 0.61 P_1$, and will be discussed in detail elsewhere (Moskalik et al., in preparation). Other discoveries from space surveys include 'period doubling', i.e. intermittent amplitude alternation (Kolenberg et al. 2010; Szabó et al. 2010), 'peculiar' RRd (pRRd) stars which have unusually low period ratios (Prudil et al. 2017; Nemec & Moskalik 2021), and various other types of Blazhko and multimode amplitude and phase modulations (Gruberbauer et al. 2007; Benkő et al. 2010, 2014; Chadid et al. 2010; Poretti et al. 2010; Nemec et al. 2011, 2013; Jurcsik et al. 2015, 2018; Smolec et al. 2015a, b, 2016, 2017a,b; Kurtz et al. 2016; Netzel & Smolec 2022; Netzel, Molnár & Joyce 2023;)

This paper presents the results of a detailed analysis of the *radial* pulsation properties of 75 RRd stars distributed around the Ecliptic Plane. The stars were observed during NASA's *K2* Mission (Howell et al. 2014; Molnár et al. 2015). Empirical relationships among the periods and amplitudes of the pulsations and the Fourier parameters are investigated. Such studies are important for identifying significant trends and correlations, which in turn, are important for the development and validation of theoretical models. For example, the Petersen diagram has, as discussed above, played a key role in understanding double-mode pulsations. Empirical studies also have many practical applications, including [Fe/H] and mass estimation.

2 K2 PHOTOMETRY

The data that were analysed are the high-precision photometric measurements made with the CCD cameras onboard NASA's *Kepler* space telescope during the *K2* Mission (Howell et al. 2014). In total more than 3000 RR Lyrae stars were observed. The stars were proposed for observation by the 'RR Lyrae and Cepheid Working Group' of the *Kepler* Asteroseismic Science Consortium (KASC), the same team that worked on the RR Lyrae stars observed in the original *Kepler*-field (Kolenberg et al. 2010; Szabó et al. 2010, 2017; Nemec et al. 2011, 2013; Moskalik et al. 2015). For a discussion of the RR Lyrae selection process see Plachy et al. (2016). The wide bandpass of the *Kepler* filter (420–900 nm), the milli-magnitude (mmag) precision of the photometry, the long (∼67–88 d) time-baseline of the continuous observations, and the short integration times (30-min for all the stars and 1-min for 17 stars) combine to make the *K2* photometry a unique and excellent data set for studying RRd stars. The *K2* observations began in 2014 February with the successful nine-day 'Two-wheel Concept Engineering Test' (see Molnár et al. 2015), and ended in 2018 September when the telescope ran out of hydrazine fuel.

A preliminary screening of the ∼3000 RR Lyrae stars observed by *K2* was conducted to identify RRd stars from including those previously not known to be RRd stars. Non-parametric methods (Lomb 1976; Stellingwerf 1978, 2011; Scargle 1982; Zechmeister & Kurster 2009; VanderPlas 2018), specifically the methods available in the `vartools` package (Hartman & Bakos 2016), were used for this purpose. This initial search provided frequency estimates for all the RR Lyrae stars. When dealing with so many stars this procedure had the advantage of being fully automatic. After the initial screening, improved pulsation periods were obtained for all candidate RRd stars using Fourier methods. The `PERIOD04` package (Lenz & Breger 2005) was employed for this purpose. In addition to identifying the main frequencies this program can be used to identify combination and alias frequencies, as well as low-amplitude non-radial frequencies.

A total of 75 RRd stars (excluding the four 'peculiar' RRd stars discussed by Nemec & Moskalik 2021) were identified from among the initial list of ∼3000 stars. Table 1 summarizes the number of RRd stars observed during each campaign. Coordinates (RA,DEC) for the stars and cross-identifications are given in Table 2. The source catalogues are: the U.S. Naval Observatory Astrograph Catalogue (DR4), `UCAC`; the Two-Micron All Sky Survey catalogue, `2MASS`; the Sloan Digital Sky Survey (DR14), `SDSS`; and the Catalina Surveys, `CSS/MLS/SSS` (see Drake et al. 2009, 2017). Star names from the `LINEAR` and `OGLE` surveys, and from the Cseresnjes (2001) study of the RR Lyrae stars in the direction of the Sagittarius dwarf galaxy, are given in Appendix A (Notes on Individual Stars). Cross-identifications with the *Gaia* catalogue (DR2, DR3) are discussed in Section 4.

2.1 *K2* long-cadence photometry

All 75 RRd stars were observed at an interval close to 29.4 min, i.e., long cadence (LC). With 49 observations per day and typical radial pulsation periods of 0.54 d (fundamental) and 0.40 d (first-overtone) the number of LC brightness measurements typically amounted to 26 fundamental and 20 first-overtone measurements per pulsation cycle. Over an 80-d campaign ∼3918 LC brightness measurements were made per star, covering 148 (fundamental) and 200 (first-overtone) pulsation cycles. The photometric measurements provided by the NASA-Ames *K2* 'Pre-Search Data Conditioning' (`PDCsap`) pipeline were usually analysed first. In all cases the photometry was found to exhibit some type of slow trend and to have a small number of outliers. After removal of obvious outliers (i.e. $>5\sigma$) the low-level trends were removed by fitting a polynomial to the flux data.

Table 1. *K2* Campaigns, observation dates and time intervals, and number of RRd stars in each field. In column (4) the numbers in parentheses are numbers of re-observed stars (see Tables 2 and 3).

K2 C	Observation dates	Duration (d) (BJD-2450000)	N(RRd)
(1)	(2)	(3)	(4)
E2	2014 Feb4-Feb13	8.9 (6693.1-6702.0)	2
C0	2014 Mar12-May27	76.7 (6728.5-6805.2)	0
C1	2014 May30-Aug20	80.0 (6810.3-6890.3)	1
C2	2014 Aug23-Nov10	77.7 (6894.3-6972.0)	1
C3	2014 Nov15-Jan23	69.2 (6977.1-7046.3)	0
C4	2015 Feb8-Apr20	69.1 (7061.8-7130.9)	4
C5	2015 Apr27-Jul10	74.6 (7139.6-7214.2)	3
C6	2015 Jul13-Sep30	78.9 (7217.5-7296.4)	4
C7	2015 Oct4-Dec26	82.6 (7300.3-7382.9)	6
C8	2016 Jan3-Mar23	78.7 (7392.1-7470.8)	4
C9	2016 Apr22-Jul02	71.3 (7501.1-7572.4)	3
C10	2016 Jul6-Sep20	69.1 (7582.6-7651.7)	6
C11	2016 Sep24-Dec08	74.2 (7656.3-7730.5)	10
C12	2016 Dec15-Mar04	78.9 (7738.4-7817.3)	3
C13	2017 Mar8-May27	80.6 (7820.6-7901.1)	1
C14	2017 May31-Aug19	79.7 (7905.7-7985.4)	12
C15	2017 Aug23-Nov20	88.0 (7989.4-8077.4)	2
C16	2017 Dec7-Feb25	79.5 (8095.5-8175.0)	1(+ 1)
C17	2018 Mar2-May08	67.1 (8179.6-8246.6)	12(+ 2)
C18	2018 May10-Jul02	50.8 (8251.6-8302.4)	0(+ 2)
C19	2018 Aug30-Sep26	26.4 (8361.1-8387.5)	0(+ 2)

All of the LC data up to and including the Campaign 6 stars as well as stars observed during Campaigns 8, 10, and 12–14 also were pre-processed (i.e. outliers removed, detrended, etc.) using the Extended Aperture Photometry (`EAP`) pipeline (see Plachy et al. 2019). An important feature of this procedure was that new apertures were created for every star using the `PyKE` software (Still & Barclay 2012). The photometric apertures contained most of the star movement within the target pixel masks but were not so large as to be contaminated by light from nearby stars. For all the photometry except that for Campaign 2 the points with `SAP_QUALITY` flags larger than 0 were removed (for Campaign 2 the large number of points with a 16384 flag were retained – this flag dominated the second half of Campaign 2 but does not affect most targets – see the Campaign 2 Data Release Notes for details.) An automated Fourier analysis script was run on the light curves to construct an initial fit, which was then subtracted from the data and all three-sigma (or more) outliers were removed. The script was then rerun on the cleaned data and this second iteration was used to derive preliminary pulsation periods and pulsation modes. Although this method produced slightly increased noise from background pixels, in many cases it preserved the pulsation amplitudes much better than either the `SAP` or `PDCsap` fluxes. For the later Campaigns (7–18) the detrending and pre-processing was done by hand using the `Pyke` software.

Table 2. Coordinates and cross-identifications for 75 RRd stars observed during NASA's *K2* Mission, ordered by *K2* campaign number and then Ecliptic Plane Input Catalogue (EPIC) number. For the three aRRd stars the EPIC numbers are given in *italics* (column 1), and the campaign numbers for stars observed at both short cadence (1-min) and long cadence (30-min) have been underlined. The very precise Right Ascension and Declination (J2000) values are from *Gaia* DR3 if available, otherwise from *Gaia* DR2 (see Table 8 for *Gaia* Identification numbers). Additional cross-identifications are given in the 'Notes on Individual Stars' (Appendix A).

Star (1)	RA (2)	DEC (3)	UCAC (4)	2MASS (5)	SDSS (6)	CSS/MLS/SSS (7)	CSS Id No. (8)
60018653 (E2)	359.1797269	+ 03.022410116	...	...	J235643.13 + 030120.2	J235643.2 + 030119	1104128004573
60018662 (E2)	355.5305737	+ 00.547990965	...	23420733 + 0032527	J234207.33 + 003252.8	J234207.3 + 003252	1101127011298
201585823 (C1)	176.83406987	+ 01.8239430144	460-049450	11472018 + 0149261	J114720.17 + 014926.2	J114720.1 + 014926	1101063037246
205209951 (C2)	239.15812379	−18.84713525	356-076676	15563794–1850494	J155637.94–185049.5	J155638.0–185049	1018082033899
210600482 (C4)	054.206234255	+ 16.972638035	...	03364949 + 1658215	J033649.49 + 165821.41	J033649.5 + 165821	1118019001177
210831816 (C4)	058.05126063	+ 20.353092411	552-007885	03521230 + 2021111	...	J035212.2 + 202111	1121020015334
210933539 (C4)	052.991116616	+ 21.920979811	560-007163	03315785 + 2155158	...	J033157.8 + 215515	1121018050281
211072039 (C4)	062.041413241	+ 24.126412764	...	04080993 + 2407349	...	J040809.9 + 240735	1123021048042
211694449 (C5,18)	126.202990	+ 15.841135	...	08244871 + 1550280	J082448.72 + 155028.2	J082448.7 + 155028	1115044045716
211888680 (C5,16)	135.59286728	+ 18.561096716	...	...	J090222.28 + 183339.9	J090222.2 + 183339	1118047037354
211898723 (C5,18)	126.10948466	+ 18.70793751	...	08242627 + 1842287	J082426.27 + 184228.6	J082426.3 + 184228	1118044044198
212335848 (C6)	201.22962833	−16.50728188	...	13245510–1630262	...	J132455.0–163026	1015070008472
212449019 (C6)	197.45153792	−13.82287849	381-064183	13094837–1349224	...	J130948.3–134920	2012179019185
212455160 (C6,17)	204.4464111	−13.6915226	...	13374714–1341294	...	J133747.0–134128	2012186019145
212547473 (C6,17)	204.20923696	−11.72830043	392-057021	13365022–1143418	...	J133650.2–114341	1012072054664
213514736 (C7)	282.6946106	−29.1564026	...	18504670–2909230	...	...	...
214147122 (C7)	282.77500119	−27.25085983	314-224182	18510600–2715029	...	...	...
229228175 (C7)	281.93738788	−28.3133953	...	...	...	...	...
229228184 (C7)	282.02556684	−29.21242517	...	...	...	...	...
229228194 (C7)	282.13188061	−29.00425155	...	...	...	...	...
229228220 (C7)	282.42495918	−25.94913418	...	...	...	...	...
220254937 (C8)	022.74793882	+ 01.6735085972	...	...	J013059.49 + 014024.6	J013059.5 + 014024	1101009031457
220604574 (C8)	018.29136574	+ 09.127136574	...	01130993 + 0907380	J011309.92 + 090737.6	J011309.9 + 090738	1109007012508
220636134 (C8)	019.791889692	+ 09.8452556167	...	...	J011910.05 + 095042.9	J011910.0 + 095043	1109007026639
229228811 (C8)	016.932617903	+ 05.9752227748	...	...	J010743.83 + 055830.7	J010743.7 + 055831	1107006006816
223051735 (C9)	271.284699	−26.588769	318-136990	18050845–2635196	...	...	...
224366356 (C9)	275.447105	−24.373911	329-142168	18214730–2422262	...	...	...
225045562 (C9)	266.691452	−23.213318	334-120104	17464595–2312479	...	...	...
201152424 (C10)	182.52057895	−05.238513136	...	12100492–0514186	...	J121004.8–051418	1004065008955
201440678 (C10)	181.21246874	−00.351834551	...	12045100–0021065	J120450.99–002106.6	J120451.0–002106	1001065053812
201519136 (C10)	185.41194533	+ 00.8164293962	...	12213890 + 0048599	J122138.86 + 004859.1	J122138.8 + 004859	1101066018344
228800773 (C10)	191.092577	−06.750381	...	...	J124422.21–064501.3	J124422.2–064501	1007068037006
228952519 (C10)	192.12454944	−02.346772672	...	...	...	J124829.9–022049	1001069010092
248369176 (C10)	185.55124222	+ 00.0526260871	...	...	J122212.29 + 000309.4	J122212.3 + 000309	1101066001707
225326517 (C11)	263.67547509	−22.72459028	...	17344233–2243295	...	...	...
225456697 (C11)	263.731894	−22.48951	338-101883	17345565–2229222	...	...	...
235631055 (C11)	259.58450133	−29.83886112	...	17182028–2950198	...	...	...
235794591 (C11)	261.90005336	−29.33767559	...	17273602–2920156	...	...	...
236212613 (C11)	258.64080782	−28.00833788	...	17143376–2800301	...	...	...
251248825 (C11)	261.74790938	−28.45405684	...	...	...	...	...
251248826 (C11)	262.16480265	−28.49276597	...	...	...	...	...
251248827 (C11)	262.4679167	−28.4059167	...	...	...	...	...
251248828 (C11)	264.6770417	−23.3172778	...	...	...	...	...
251248830 (C11)	266.0330417	−25.9605278	...	...	...	...	...
245974758 (C12,19)	349.306822	−10.148914	...	23171363–1008560	J231713.66–100855.9	J231713.6–100855	1009124026999
246058914 (C12,19)	351.42089314	−08.049997582	...	23254104–0803002	J232541.00–080259.8	J232540.9–080259	1007124007872
251456808 (C12)	350.4464167	+ 00.2357222	...	...	J232147.14 + 001408.6	J232147.2 + 001408	1101125004451
247334376 (C13)	078.638079082	+ 20.852896452	...	05143315 + 2051098	...	J051433.1 + 205110	1121027045355
201749391 (C14)	165.264565	+ 04.472659	473-046469	11010348 + 0428214	J110103.49 + 042821.6	J110103.5 + 042821	1104059033335
248426222 (C14)	160.48146706	+ 00.5889994022	...	10415554 + 0035202	J104155.55 + 003520.4	J104155.6 + 003520	1101058012922
248509474 (C14)	158.3716221	+ 03.4408391135	...	10332919 + 0326271	J103329.19 + 032627.0	J103329.2 + 032627	1104057013286
248514834 (C14)	157.53471727	+ 03.6022996457	469-043448	10300833 + 0336084	J103008.33 + 033608.2	J103008.3 + 033608	1104057016830
248653210 (C14)	158.52769285	+ 07.2022393032	...	...	J103406.64 + 071208.0	J103406.6 + 071207	1107056030993
248653582 (C14)	160.49248756	+ 07.2116772807	487-051343	10415821 + 0712422	J104158.19 + 071242.0	J104158.2 + 071242	1107057030584
248667792 (C14)	157.14515297	+ 07.5659142694	...	10283482 + 0733567	J102834.83 + 073357.3	J102834.8 + 073357	1107056038736
248730795 (C14)	160.16983198	+ 09.0358273696	496-056499	10404076 + 0902089	J104040.76 + 090209.0	...	...
248731983 (C14)	160.77562409	+ 09.0612043096	496-056556	10430615 + 0903405	J104306.15 + 090340.3	...	...
248827979 (C14)	155.557981	+ 11.355388	...	10221391 + 1121193	J102213.92 + 112119.4	...	...
248845745 (C14)	160.43736748	+ 11.796589092	...	...	J104144.96 + 114747.7	...	...
248871792 (C14)	162.66135792	+ 12.457650633	513-052553	10503874 + 1227276	J105038.73 + 122727.6	...	...
249790928 (C15)	234.3329736	−18.01575394	360-074594	15371992–1800567	...	J153719.9–180056	1018081063248
250056977 (C15)	234.77375229	−14.80469274	...	15390570–1448168	J153905.70–144816.8	J153905.8–144816	1015081070790
211665293 (C16)	136.01875492	+ 15.444972769	528-049596	09040449 + 1526417	J090404.49 + 152642.0	J090404.5 + 152642	1115047028617
212467099 (C17)	199.90526047	−13.43885865	...	13193728–1326195	...	J131937.3–132619	1012070013928
212498188 (C17)	204.4953766	−12.7721872	...	13375888–1246198	...	J133758.9–124619	1012072031579
212615778 (C17)	198.42722343	−10.2322055	...	13134252–1013557	...	J131342.5–101356	1009071023139
212819285 (C17)	207.0258789	−04.9317350	...	...	J134806.20–045554.2	J134806.2–045554	1004074016553
251521080 (C17)	196.93288681	−03.280491255	...	...	J130743.89–031649.7	J130743.8–031641	1004071051158
251629085 (C17)	199.52759172	−00.550094147	448-055695	13180662-0033002	J131806.62–003300.2	J131806.6–003300	1001071051356
251809772 (C17)	204.6996200	−08.5891100	...	...	...	J133847.9–083520	2008188002549
251809814 (C17)	201.8208117	−05.6359357	...	...	...	J132716.9–053809	1004072000498
251809825 (C17)	204.43143696	−07.755244459	...	...	...	J133743.5–074518	1007073015747
251809832 (C17)	204.83307773	−13.67106856	...	...	...	J133920.0–134016	1012072010870
251809860 (C17)	201.4751985	−01.0399776	...	...	J132554.04–010224.0	J132553.9–010222	1001072041910
251809870 (C17)	207.1282046	−12.2034152	...	...	...	J134830.9–121210	1012073044969

2.2 *K2* short-cadence photometry

In addition to the long-cadence observations, 17 of the RRd stars were also observed at a sampling rate of (29.4/30=) 0.98 min, i.e. short cadence (SC). These data permit the detection of high frequencies, up to the SC Nyquist frequency of 734.7 d^{-1} (or equivalently, periods as short as two minutes). For frequencies lower than the LC Nyquist frequency the frequencies detectable are similar for the SC and LC data. Where the two data sets differ is in the background noise levels of the amplitude spectra: the SC data tend to have higher signal-to-noise ratio peaks than the LC data, and hence are more suitable for the detection of low-amplitude frequencies (such as non-radial modes). In Table 2 (and elsewhere throughout this paper) the EPIC numbers of stars with SC data have been underlined. During Campaign 14 six of the 15 stars were observed at SC; the other eight stars with SC data were observed during seven other campaigns. To take advantage of the more frequent sampling offered by the SC data, brightness measurements were also made using the PyKE software. Apertures larger than the PDCSAP apertures were defined for each star (as for the EAP pipeline) and aperture photometry was performed. To minimize outliers all data points with SAPQUALITY flags greater than zero were excluded from the analysis. EPIC 205209951 is the only star with SC data that is not a classical RRd star; it lies below the cRRd curve in the Petersen diagram, exhibits distinct Blazhko modulations (see Plachy et al. 2017), and is an aRRd star similar to those found in Messier 3 and in the Magellanic Clouds.

3 ANALYSIS OF K2 PHOTOMETRY

Fourier amplitude spectra (Period04) for EPIC 201585823, which is a classical RRd star observed during Campaign 1, are shown in Fig. 3. This star has SC data and was studied in detail by Kurtz et al. (2016). The figure illustrates the considerably better quality of the *K2* photometry (top panel) compared with earlier ground-based observations made by the LINEAR Survey (middle panel) and by the Catalina Sky Survey (bottom panel). All three data sets show peaks at the dominant first-overtone (f_1) and fundamental-mode (f_0) frequencies. For the K2 data the two radial pulsation components have Fourier 1st-term amplitudes A_1(Kp)∼180 mmag for the first-overtone and A_0(Kp)∼90 mmag for the fundamental mode (see Table 3). Only the *K2* spectrum is of sufficient quality to detect low amplitude peaks due to combinations of these two frequencies and the even lower amplitude peak of the non-radial pulsation. The non-radial frequency (labelled f_{nr}) at 4.5154(±1) d^{-1} with amplitude 5.24 ± 0.18 mmag is barely visible at the scale shown. At higher resolution the background level of the *K2* data in the vicinity of this non-radial peak is seen to be ∼0.2 mmag and thus the signal-to-noise ratio of the peak is high, ∼30, despite its low amplitude. The numbers given here are consistent with those found by Kurtz et al. (2016).

Detrended photometry and fitted light curves for the 'classical' RRd stars observed during Campaigns 1–6 of the *K2* Mission are plotted in Fig. 4. For each star only the first five days of the available data are shown. Panel labels give the EPIC number and the *K2* campaign number in which the star was observed. The smooth fitted curves (green lines) illustrate the quality of the Period04 analysis for each star. Typically more than 25 frequencies were included in the least-squares fits with the brightest stars usually revealing the greatest number of significant frequencies. In addition to the independent radial frequencies, many of the detected periodicities are harmonics that describe the non-sinusoidal nature of the light

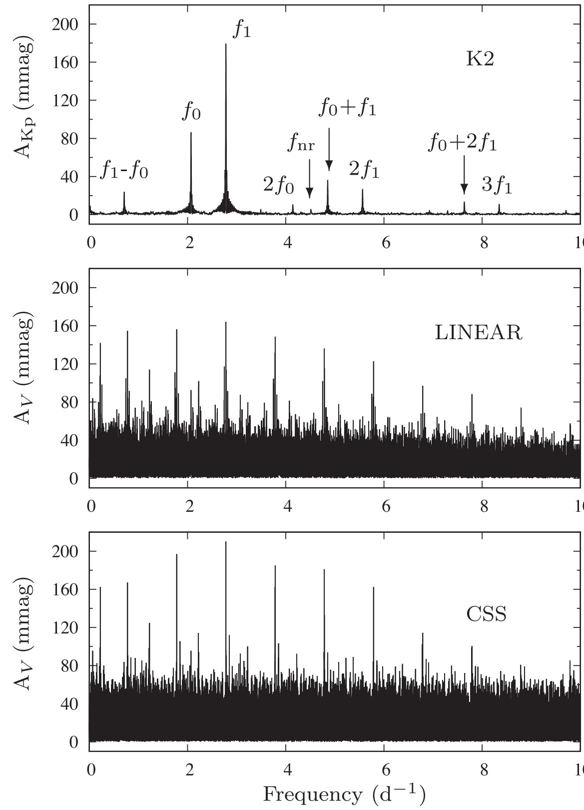

Figure 3. Fourier amplitude spectra for EPIC 201585823 (C1): (Top) the *K2* photometry (3671 brightness measurements made over 80 d); (Middle) the LINEAR Survey data (519 observations made over 5.5 yr with no filter and transformed to the *V*-passband); (Bottom) the Catalina Sky Survey data (354 CSS and 243 MLS photometric observations over 8.2 yr).

curves of the individual modes or observational aliases (for example, due to the thruster firings every six hours). In addition, combination frequencies involving the two radial modes are commonly detected. In general the fits are exceptionally good with root-mean-squared errors ranging from 5 to 100 mmag depending on the quality of the photometry.

Light curves for the RRd stars observed during Campaigns 7–18 are given in Appendix B. The graphs illustrate the similarities and differences seen in the light curves for the various stars and campaigns. These include photometric variations from star to star and from one campaign to the next, gaps in the data, systemic brightness differences, cycle-to-cycle differences that could not previously be seen in earlier ground-based observations, etc.

Our best estimates of the pulsation periods and amplitudes (fundamental and first-overtone radial modes) for the *K2* RRd stars are given in Table 3. Mean magnitudes, useful for distance estimation and for planning follow-up spectroscopy, are given in columns 2–5. The *V* magnitudes (column 2) are from previously published ground-based photometry. The *G* magnitudes (column 3) are from the *Gaia* mission (from DR3 if available, otherwise DR2). For the Campaign 7 RRd stars in the direction of the Sagittarius dwarf galaxy (see Appendix A) the *V* magnitudes were estimated by subtracting 0.30 mag from the mean *B* magnitudes given by Cseresnjes (2001). The *Kp* magnitudes given at the MAST website (column 4) are from Huber et al. (2016) and were derived using previous IR and other photometry. The *Kp* magnitudes labelled '*K2*' (column 5) were derived from the present analysis using the *K2* light curves and the

Table 3. Mean magnitudes, pulsation periods, and amplitudes for the 72 cRRd and three aRRd stars observed during the *K2* Mission (ordered by increasing pulsation period). Column (1) contains EPIC identification numbers and, in parentheses, the *K2* campaign(s) in which the star was observed (an underlined campaign number indicates that short-cadence photometry was analysed). The mean magnitudes are through the *V* filter (column 2), the *Gaia* G-filter (column 3), and the *Kepler* filter, where the *Kp* magnitudes in column (4) are from the MAST catalogue (Huber et al. 2016), and those in column (5) are from the present analysis. Columns (6)–(9) contain first-overtone and fundamental-mode periods, respectively, and Fourier first-term amplitudes. For the stars observed during Campaigns 9 and 11 the adopted periods are the very precise values from the OGLE-IV (2010-17) survey, and the associated amplitudes are from the high-precision *K2* photometry (this paper). Columns (10) and (11) give ratios of the periods and amplitudes. Empty rows in the table separate stars with multiple observations (LC, SC, multiple campaigns) from those with LC observations only.

EPIC No. (1)	⟨V⟩ (mag) (2)	⟨G⟩ *Gaia* (3)	⟨Kp⟩ MAST (4)	⟨Kp⟩ *K2* (5)	P_1 (d) (6)	A_1(Kp) (mmag) (7)	P_0 (d) (8)	A_0(Kp) (mmag) (9)	P_1/P_0 (10)	A_1/A_0 (11)
(a) 'Classical' RRd (cRRd) stars										
225456697 (C11)	16.84	...	[14.50]	16.85	0.2943527(±1)	97.5 ± 0.4	0.3998380(±4)	53.4 ± 0.4	0.73618(±1)	1.82 ± 0.02
251248830 (C11)	19.9:	...	19.86	20.29	0.310017(±8)	225.7 ± 3.7	0.419592(±14)	235.4 ± 3.7	0.73886(±4)	0.96 ± 0.03
251248826 (C11)	19.57	[18.59]	19.53	19.60	0.3182948(±2)	206.0 ± 1.2	0.430234(±1)	54.2 ± 1.2	0.73982(±1)	3.80 ± 0.10
246058914 (C12)	17.00	16.94	16.89	17.02	0.336110(±1)	169.3 ± 0.3	0.452948(±2)	176.6 ± 0.3	0.74205(±1)	0.959(±3)
246058914 (C12)				16.97	0.3361100(±4)	169.3 ± 0.1	0.4529476(±7)	174.3 ± 0.1	0.74205(±1)	0.971(±1)
251248827 (C11)	19.04	...	19.07	19.02	0.3379169(±1)	190.4 ± 0.9	0.4552683(±2)	187.0 ± 0.9	0.74224(±1)	1.018(±9)
229228184 (C7)	18.80	18.13	18.10	18.79	0.34105(±2)	182.0 ± 2.7	0.45943(±4)	132.6 ± 2.7	0.7423(±1)	1.37 ± 0.05
224366356 (C9)	17.96	...	[14.57]	17.99	0.3430486(±4)	112.0 ± 1.3	0.4619359(±6)	105.7 ± 1.9	0.74263(±2)	1.06 ± 0.03
251629085 (C17)	15.89	15.91	15.87	16.14	0.344183(±4)	164.6 ± 0.6	0.46311(±4)	25.9 ± 0.6	0.74319(±6)	6.36 ± 0.18
201519136 (C10)	16.94	16.97	17.95	17.03	0.344312(±2)	171.5 ± 0.3	0.463376(±4)	139.9 ± 0.3	0.74305(±1)	1.23 ± 0.01
211694449 (C5)	17.27	...	18.18	17.43	0.3443615(±10)	177.0 ± 0.3	0.463655(±2)	195.3 ± 0.3	0.74271(±1)	0.91 ± 0.01
211694449 (C18)				17.33	0.344362(±2)	165.0 ± 0.3	0.463655(±3)	180.0 ± 0.3	0.74271(±1)	0.92 ± 0.01
211694449 (C18)				17.31	0.3443606(±8)	161.5 ± 0.1	0.4636518(±9)	176.5 ± 0.1	0.74271(±1)	0.915(±1)
211694449 (C5,18)				17.33	0.34436220(±4)	172.2 ± 0.3	0.4636503(±1)	189.1 ± 0.3	0.74272(±1)	0.91 ± 0.01
251809814 (C17)	19.00	...	18.99	19.23	0.347284(±3)	228.1 ± 0.7	0.467124(±6)	169.0 ± 0.7	0.74345(±2)	1.35 ± 0.01
251456808 (C12)	20.1	...	19.80	20.31	0.348582(±9)	136.1 ± 1.9	0.46898(±2)	104.6 ± 1.9	0.74328(±5)	1.30 ± 0.04
212615778 (C17)	17.02	17.01	[17.98]	17.10	0.3488887(±11)	172.4 ± 0.2	0.469391(±2)	141.7 ± 0.2	0.74328(±1)	1.216(±4)
236212613 (C11)	18.00	17.57	[16.90]	18.00	0.3489577(±2)	142.5 ± 0.6	0.4692002(±4)	84.7 ± 0.6	0.74373(±1)	1.68 ± 0.02
212455160 (C6)	17.23	...	17.98	17.40	0.349321(±1)	187.2 ± 0.4	0.469592(±4)	125.3 ± 0.3	0.74388(±1)	1.49 ± 0.01
212455160 (C17)				17.40	0.349316(±10)	149.5 ± 1.4	0.46950(±2)	103.0 ± 1.4	0.74374(±9)	1.45 ± 0.03
212455160 (C6,17)				17.38	0.3493208(±14	184.2 ± 0.3	0.469592(±4)	123.7 ± 0.3	0.74388(±1)	1.49 ± 0.01
229228175 (C7)	19.30	18.47	18.60	18.86	0.349452(±11)	141.0 ± 1.4	0.46954(±5)	35.4 ± 1.4	0.7443(±1)	3.99 ± 0.19
248653210 (C14)	17.89	17.80	17.65	18.05	0.350434(±2)	189.6 ± 0.5	0.471007(±6)	101.9 ± 0.5	0.74401(±1)	1.86 ± 0.02
245974758 (C12)	17.01	...	17.68	17.13	0.353309(±2)	167.1 ± 0.5	0.475291(±5)	125.3 ± 0.5	0.74335(±2)	1.334(±9)
245974758 (C12)				17.13	0.3533078(±4)	171.7 ± 0.1	0.475291(±1)	127.9 ± 0.1	0.74335(±1)	1.342(±2)
212819285 (C17)	19.1	...	19.10	19.3	0.353446(±4)	185.7 ± 0.8	0.474968(±13)	96.7 ± 0.8	0.74415(±3)	1.92 ± 0.02
251809825 (C17)	19.2	19.15	19.21	19.59	0.353727(±3)	193.0 ± 0.7	0.475900(±8)	137.2 ± 0.7	0.74328(±2)	1.41 ± 0.01
220604574 (C8)	17.33	17.40	17.69	17.43	0.354733(±1)	188.2 ± 0.2	0.476772(±7)	48.7 ± 0.2	0.74403(±1)	3.87 ± 0.02
251809772 (C17)	19.0	...	18.84	19.16	0.355035(±3)	174.4 ± 0.5	0.477332(±6)	119.4 ± 0.5	0.74379(±2)	1.46 ± 0.01
212335848 (C6)	17.03	17.09	17.80	17.36	0.355068(±2)	169.6 ± 0.3	0.476856(±6)	69.6 ± 0.3	0.74460(±1)	2.44 ± 0.02
201749391 (C14)	15.74	...	15.84	15.73	0.3573202(±7)	180.7 ± 0.2	0.479940(±2)	112.3 ± 0.2	0.74451(±1)	1.609(±4)
201749391 (C14)				15.79	0.3573249(±3)	176.5 ± 0.1	0.479930(±1)	108.7 ± 0.1	0.74454(±1)	1.624(±1)
248845745 (C14)	...	17.94	17.94	18.00	0.358376(±2)	179.3 ± 0.4	0.481123(±8)	58.9 ± 0.4	0.74487(±2)	3.04 ± 0.03
201152424 (C10)	17.52	17.63	18.17	17.65	0.358500(±2)	179.5 ± 0.3	0.481725(±9)	44.7 ± 0.3	0.74420(±2)	4.02 ± 0.04
210933539 (C4)	14.97	15.16	15.22	15.18	0.358617(±2)	165.3 ± 0.3	0.481800(±4)	119.8 ± 0.3	0.74433(±1)	1.379(±6)
210933539 (C4)				15.20	0.3586161(±2)	163.3 ± 0.1	0.4818008(±5)	117.6 ± 0.1	0.74432(±1)	1.389(±1)
248667792 (C14)	17.43	17.47	17.81	17.56	0.358942(±1)	177.5 ± 0.3	0.482054(±4)	95.3 ± 0.3	0.74461(±1)	1.862(±8)
211888680 (C5)	18.74	18.80	18.83	18.91	0.359375(±3)	175.6 ± 0.5	0.482994(±7)	108.6 ± 0.5	0.74406(±2)	1.62 ± 0.01
211888680 (C16)				19.00	0.359383(±2)	176.6 ± 0.5	0.482994(±6)	107.1 ± 0.5	0.74407(±1)	1.65 ± 0.01
211888680 (C5,16)				19.00	0.3593838(±1)	176.0 ± 0.3	0.4829926(±2)	107.8 ± 0.3	0.74408(±1)	1.63 ± 0.01
201585823 (C1)	15.79	15.75	15.83	15.73	0.3594198(±7)	181.4 ± 0.2	0.482591(±2)	88.7 ± 0.2	0.74477(±1)	2.046(±5)
201585823 (C1)				15.73	0.3594190(±2)	179.7 ± 0.1	0.4825903(±6)	87.7 ± 0.1	0.74477(±1)	2.050(±1)
210600482 (C4)	17.21	17.35	17.64	17.45	0.362471(±1)	177.6 ± 0.3	0.487191(±3)	117.4 ± 0.3	0.74400(±1)	1.513(±5)
229228220 (C7)	19.9	18.89	19.20	19.20	0.363387(±6)	119.4 ± 0.9	0.48774(±3)	31.0 ± 0.9	0.74505(±5)	3.85 ± 0.14
212449019 (C6)	16.32	16.49	16.32	16.55	0.363388(±1)	152.5 ± 0.2	0.487778(±6)	57.8 ± 0.2	0.74499(±1)	2.64 ± 0.02
251809860 (C17)	20.1	...	20.18	20.93	0.363480(±8)	235.3 ± 2.0	0.488442(±19)	162.3 ± 2.0	0.74416(±4)	1.45 ± 0.03
210831816 (C4)	15.38	15.57	15.85	15.56	0.3638034(±9)	175.4 ± 0.2	0.488793(±6)	42.8 ± 0.2	0.74429(±1)	4.09 ± 0.02
211665293 (C16)	16.51	16.49	16.60	16.50	0.366065(±1)	181.0 ± 0.2	0.491516(±4)	64.3 ± 0.2	0.74477(±1)	2.82 ± 0.01
212498188 (C17)	17.0	...	17.74	17.16	0.371357(±2)	170.2 ± 0.3	0.498643(±4)	137.1 ± 0.3	0.74473(±1)	1.24 ± 0.01
228800773 (C10)	18.03	...	18.26	17.72	0.372744(±4)	131.2 ± 0.5	0.49988(±1)	70.7 ± 0.5	0.74566(±2)	1.86 ± 0.02
229228811 (C8)	17.95	18.03	17.70	18.14	0.372911(±2)	179.5 ± 0.3	0.500219(±6)	78.7 ± 0.3	0.74550(±1)	2.28 ± 0.01
251521080 (C17)	18.0	17.97	17.75	18.36	0.373014(±5)	141.7 ± 0.7	0.50087(±2)	94.3 ± 0.7	0.74473(±3)	1.50 ± 0.02
220636134 (C8)	17.09	17.22	17.30	17.36	0.373741(±2)	174.7 ± 0.4	0.501370(±6)	91.8 ± 0.4	0.74544(±1)	1.90 ± 0.01
220636134 (C8)				17.17	0.3737393(±7)	164.0 ± 0.1	0.501375(±2)	85.6 ± 0.1	0.74543(±1)	1.917(±4)

Table 3 – *continued*

EPIC No. (1)	⟨V⟩ (mag) (2)	⟨G⟩ *Gaia* (3)	⟨Kp⟩ MAST (4)	⟨Kp⟩ *K2* (5)	P_1 (d) (6)	A_1(Kp) (mmag) (7)	P_0 (d) (8)	A_0(Kp) (mmag) (9)	P_1/P_0 (10)	A_1/A_0 (11)
213514736 (C7)	17.6	...	17.30	17.46	0.375213(±4)	177.7 ± 0.5	0.503583(±9)	129.1 ± 0.5	0.74509(±2)	1.376(±9)
251809870 (C17)	20.4	...	20.45	20.08	0.375881(±14)	94.3 ± 1.6	0.50483(±3)	83.7 ± 1.6	0.74457(±9)	1.13 ± 0.04
248871792 (C14)	15.2	15.23	14.95	15.36	0.376317(±2)	177.2 ± 0.3	0.505491(±3)	143.1 ± 0.3	0.74446(±1)	1.238(±5)
248871792 (C14)				15.34	0.3763140(±2)	177.1 ± 0.1	0.5054967(±4)	142.2 ± 0.1	0.74444(±1)	1.245(±1)
211898723 (C5)	17.01	16.98	17.49	17.03	0.376514(±1)	173.3 ± 0.2	0.505825(±3)	121.1 ± 0.2	0.74436(±6)	1.43 ± 0.01
211898723 (C5)				16.97	0.376512(±1)	169.5 ± 0.1	0.505813(±1)	119.0 ± 0.1	0.74437(±1)	1.425(±2)
211898723 (C18)				16.98	0.376509(±2)	172.3 ± 0.3	0.505847(±6)	114.1 ± 0.3	0.74431(±1)	1.51 ± 0.01
211898723 (C5,18)				17.03	0.3765109(±1)	172.9 ± 0.2	0.5058274(±1)	118.4 ± 0.2	0.74435(±1)	1.46 ± 0.01
201440678 (C10)	17.03	17.01	17.24	17.14	0.376676(±2)	178.1 ± 0.4	0.505614(±11)	60.6 ± 0.4	0.74499(±2)	2.94 ± 0.3
212467099 (C17)	16.79	16.77	17.46	17.09	0.386354(±3)	184.5 ± 0.4	0.517170(±18)	45.8 ± 0.4	0.74705(±3)	4.03 ± 0.05
251809832 (C17)	19.5	19.47	19.48	19.45	0.387565(±5)	162.1 ± 0.8	0.51919(±3)	38.1 ± 0.8	0.74648(±6)	4.25 ± 0.11
229228194 (C7)	18.9	18.08	18.10	19.3	0.38971(±2)	[267]	0.52263(±10)	[166]	0.7457(±2)	[1.6]
248827979 (C14)	...	...	17.69	17.69	0.389714(±8)	170.6 ± 0.6	0.522807(±10)	114.8 ± 0.6	0.74543(±2)	1.49 ± 0.02
248730795 (C14)	16.1	16.03	16.10	16.11	0.390117(±1)	185.2 ± 0.2	0.522545(±6)	62.6 ± 0.2	0.74657(±1)	2.96 ± 0.02
211072039 (C4)	16.84	17.07	16.80	17.19	0.393491(±2)	168.8 ± 0.4	0.527041(±11)	57.2 ± 0.4	0.74660(±2)	2.95 ± 0.03
250056977 (C15)	16.04	16.39	16.47	16.44	0.396746(±2)	149.7 ± 0.4	0.532607(±5)	112.5 ± 0.4	0.74491(±1)	1.330(±9)
250056977 (C15)				16.54	0.3967475(±2)	152.7 ± 0.1	0.532603(±1)	114.5 ± 0.1	0.74492(±1)	1.334(±1)
220254937 (C8)	17.91	17.89	17.89	18.22	0.400127(±3)	182.0 ± 0.6	0.535934(±15)	57.1 ± 0.6	0.74660(±3)	3.19 ± 0.05
248426222 (C14)	17.24	17.17	17.20	17.46	0.401116(±3)	179.2 ± 0.5	0.537644(±8)	97.0 ± 0.5	0.74606(±2)	1.85 ± 0.02
060018653 (E2)	14.21	14.52	...	13.72	0.402311(±16)	139.9 ± 0.4	0.539427(±90)	46.4 ± 0.4	0.74581(±3)	3.01 ± 0.03
060018653 (E2,css)				14.21	0.4023084(±4)	115.7 ± 3.6	0.539441(±1)	59.5 ± 3.6	0.74579(±1)	1.90 ± 0.20
248653582 (C14)	14.90	14.76	14.96	14.94	0.4027260(±8)	168.2 ± 0.1	0.539881(±3)	88.6 ± 0.2	0.74595(±1)	1.899(±4)
248653582 (C14)				14.95	0.4027261(±2)	166.4 ± 0.0	0.5398778(±5)	86.8 ± 0.1	0.74596(±1)	1.918(±1)
247334376 (C13)	17.51	18.11	17.57	18.32	0.403243(±9)	164.6 ± 1.4	0.53958(±4)	26.0 ± 1.4	0.74732(±7)	6.34 ± 0.39
228952519 (C10)	17.76	18.06	18.19	17.90	0.40349(±7)	142.0 ± 4.0	0.5406(±15)	37.0 ± 7.0	0.7464(±22)	3.8 ± 0.8
214147122 (C7)	16.8	15.83	15.83	15.90	0.403657(±3)	158.6 ± 0.3	0.541040(±14)	68.7 ± 0.3	0.74608(±3)	2.31 ± 0.02
235794591 (C11)	17.38	16.72	15.87	17.38	0.4040492(±1)	169.6 ± 0.6	0.5415829(±5)	61.7 ± 0.6	0.74605(±1)	2.75 ± 0.03
251248825 (C11)	19.63	[18.68]	19.62	19.61	0.4041701(±2)	141.3 ± 0.6	0.5413433(±9)	40.5 ± 0.6	0.74661(±1)	3.49 ± 0.07
212547473 (C6)	15.59	15.68	16.16	15.94	0.406430(±1)	187.3 ± 0.2	0.545079(±4)	90.6 ± 0.2	0.74563(±1)	2.07 ± 0.01
212547473 (C6)				15.74	0.4064318(±2)	173.5 ± 0.1	0.5450751(±8)	82.7 ± 0.1	0.74564(±1)	2.10 ± 0.01
212547473 (C17)				15.75	0.4064217(±13)	173.5 ± 0.2	0.545069(±5)	77.5 ± 0.2	0.74563(±1)	2.24 ± 0.01
212547473 (C17)				15.74	0.4064214(±3)	174.2 ± 0.1	0.545067(±1)	77.4 ± 0.1	0.74564(±1)	2.25 ± 0.01
212547473 (C6,17)				15.74	0.40643852(±1)	173.8 ± 0.1	0.5450887(±1)	80.1 ± 0.1	0.74564(±1)	2.17 ± 0.01
248509474 (C14)	16.76	16.74	16.64	16.84	0.415104(±4)	167.5 ± 0.4	0.557304(±15)	109.0 ± 0.4	0.74484(±2)	1.54 ± 0.01
248509474 (C14)				16.80	0.4151037(±4)	166.3 ± 0.1	0.557312(±1)	106.4 ± 0.1	0.74483(±2)	1.563(±1)
060018662 (E2)	14.74	14.77	...	14.22	0.417448(±47)	167.8 ± 0.8	0.55900(±23)	60.7 ± 0.9	0.7468(±4)	2.76 ± 0.05
060018662 (E2,css)				14.22	0.4175081(±3)	168.4 ± 2.9	0.559323(±1)	55.2 ± 2.9	0.74645(±1)	3.05 ± 0.21
248731983 (C14)	...	13.68	13.81	13.77	0.4175015(±11)	171.5 ± 0.2	0.560084(±4)	84.7 ± 0.2	0.74543(±1)	2.03 ± 0.01
248731983 (C14)				13.74	0.4175000(±1)	170.8 ± 0.1	0.5600838(±5)	82.8 ± 0.1	0.74542(±1)	2.063(±1)
223051735 (C9)	16.50	...	[13.47]	16.50	0.4233213(±2)	164.2 ± 2.2	0.5677371(±7)	78.8 ± 2.3	0.74563(±1)	2.08 ± 0.09
248369176 (C10)	20.40	20.20	19.90	20.36	0.424078(±10)	177.1 ± 1.5	0.56828(±3)	75.3 ± 1.5	0.74625(±6)	2.35 ± 0.07
249790928 (C15)	14.51	14.56	14.71	14.58	0.4306134(±9)	162.7 ± 0.1	0.578550(±6)	40.7 ± 0.1	0.74430(±1)	4.00 ± 0.02
235631055 (C11)	18.19	17.48	[16.93]	18.15	0.4327289(±2)	192.2 ± 1.0	0.5804633(±7)	84.1 ± 1.0	0.74549(±1)	2.29 ± 0.04
225326517 (C11)	17.71	17.12	[16.11]	17.69	0.4335412(±2)	171.7 ± 0.4	0.581816(±1)	45.7 ± 0.4	0.74515(±1)	3.76 ± 0.04
248514834 (C14)	15.5	15.47	15.44	15.55	0.434419(±2)	162.4 ± 0.2	0.581294(±10)	40.5 ± 0.1	0.74733(±2)	4.01 ± 0.02
248514834 (C14)				15.55	0.4344186(±2)	160.1 ± 0.1	0.581287(±2)	39.6 ± 0.1	0.74734(±1)	4.044(±3)
(b) 'Anomalous' RRd (aRRd) stars										
251248828 (C11)	18.84	...	18.87	18.87	0.32064461(±4)	70.3 ± 1.0	0.4419347(±5)	95.0 ± 1.0	0.72555(±1)	0.74 ± 0.02
225045562 (C9)	17.97	...	[13.69]	18.12	0.34061(±2)	167.0 ± 5.0	0.4636(±1)	111.0 ± 5.0	0.7347(±2)	1.50 ± 0.11
205209951 (C2)	14.43	14.69	14.91	14.70	0.348780	15-160	0.470741	60-370	0.74092	0.1-2.3

flux-to-magnitude calibration given by Lund et al. (2015): $Kp = 25.3 - 2.5\log_{10}F$, where F is the median of the flux time series (units of e^{-}/s). The mean fluxes, which range from around 50 000 e^{-}/s to fewer than 100 e^{-}/s, depend on the size of the aperture and come from either the EAP pipeline, the PDCSAP estimates calculated by the *K2* pipeline, or from our own analyses using the PYKE software. In most cases the mean magnitudes in columns 2–5 are similar, with brightnesses ranging from 14.2 mag (EPIC 60018653) to 20.4 mag (EPIC 248369176). Outliers are identified with square brackets. The largest discrepancies are for stars in the crowded Galactic Bulge fields (Campaigns 9 and 11). The procedure for calculating the periods and amplitudes in Table 3 was similar to that used in our analysis of peculiar RRd stars (NM21). For this paper an additional term was added to the model to represent non-radial oscillations with periods

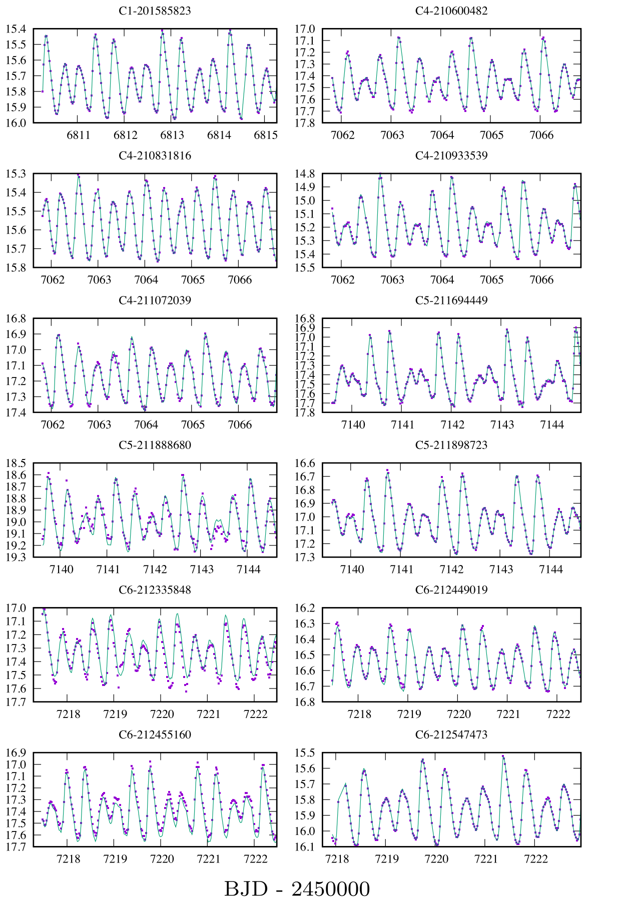

Figure 4. Observed *Kepler* Kp photometry and fitted light curves for the 12 'classical' RRd stars observed during Campaigns 1-6 of the *K2* Mission. The observed Kp magnitudes were derived using the long-cadence fluxes (e^{-}/s, `EAP` pipeline) transformed to magnitudes using Kp = 25.3 − 2.5log *F*. Only the first five days of data are shown, and the fits were made using `Period04`.

$P_{\rm nr}$ near 0.61 P_1 (see Moskalik et al. 2018a,b):

$$\begin{aligned} m(t) = m_0 &+ \sum_{i=1}^{N_1} A_{\rm i,1} \sin\left(i\omega_1\,[t-t_0] + \phi_{\rm i,1}\right) \\ &+ \sum_{j=1}^{N_0} A_{\rm j,0} \sin\left(j\omega_0\,[t-t_0] + \phi_{\rm j,0}\right) \\ &+ \sum_{k=1}^{N_{\rm nr}} A_{\rm k,nr} \sin\left(k\omega_{\rm nr}\,[t-t_0] + \phi_{\rm k,nr}\right) \\ &+ \sum_{i=1}^{N_1}\sum_{j=1}^{N_0} [A^{+}_{\rm i,j} \sin\left((i\omega_1 + j\omega_0)\,[t-t_0] + \phi^{+}_{\rm i,j}\right) \\ &+ A^{-}_{\rm i,j} \sin\left((i\omega_1 - j\omega_0)\,[t-t_0] + \phi^{-}_{\rm i,j}\right)], \end{aligned} \qquad (1)$$

where m_0 is the mean magnitude; ω_1, ω_0, and $\omega_{\rm nr}$ are the angular frequencies for the first-overtone, fundamental, and non-radial modes; the A and ϕ are the amplitudes and phases of the various terms in the Fourier sums; and N_1, N_0, and $N_{\rm nr}$ are, respectively, the number of terms for the (usually dominant) first-overtone, the fundamental and the non-radial modes that were included in the expansion. Values for N_1, N_0, and $N_{\rm nr}$ were adjusted to include all significant harmonic peaks (typically five harmonics were included) in the amplitude spectra. The multifrequency model (equation 1) was fitted by non-linear (Levenberg-Marquardt) least-squares using the `PROC NONLIN` procedure in SAS© version 9.4 (SAS Institute Inc. 2014).

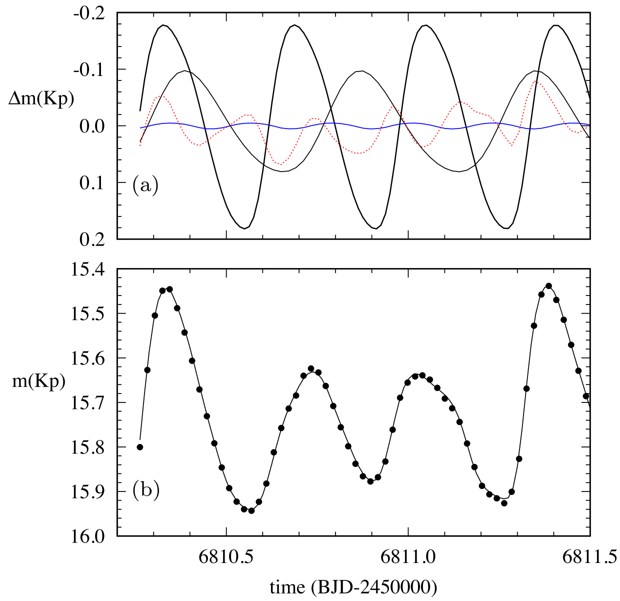

Figure 5. Component light curves for the 'classical' RRd star EPIC 201585823. Non-linear least-squares fitting of the EAP photometry was used to estimate the Fourier parameters, and for clarity only the first 1.2 d of data are plotted. Upper panel: the highest amplitude, slightly asymmetric curve with Fourier 1st-term amplitude A_1(Kp) = 181.4 mmag is for the first-overtone with P_1 = 0.3594190 d; the second largest amplitude curve with A_0(Kp) = 88.7 mmag is for the fundamental mode with P_0 = 0.4825903 d; the lowest amplitude curve with $A_{\rm nr}$(Kp) = 5.3 mmag is for the non-radial mode with $P_{\rm nr}$ = 0.22146 d; and the dotted curve is the variable amplitude contribution from the P_1 and P_0 combination frequencies. Lower panel: comparison of the observed *K2* photometry (dots) with the predicted light curve (equal to the sum of the four curves shown in the top panel).

Fig. 5 shows the component light curves (upper panel) and their sum (lower panel), for EPIC 201585823.[1] The amplitude spectrum (shown in Fig. 3) clearly identifies the main frequencies as the radial first-overtone mode (dominant) and the radial fundamental mode (secondary). The next most significant contribution comes from the combination terms involving the two radial modes (red dotted curve in Fig. 5); these are seen to contribute more to the summed light curve than the low amplitude non-radial component (blue light curve). When all the terms are added (lower panel) the standard deviation of the residuals amounts to only σ = 6.6 mmag.

The derived amplitudes and phases were used to calculate two sets of Fourier decomposition parameters (Simon & Lee 1981; Simon 1990) for the *K2* light curves: epoch(t_0)-independent phase differences $\phi_{\rm i1} = \phi_i - i\phi_1$ and amplitude ratios $R_{\rm i1} = A_i/A_1$, where i denotes the ith harmonic. In Table 4 these quantities (for i = 2,3) are given for the radial first-overtone component, and in Table 5 for the radial fundamental mode. In both tables column (3) contains the pulsation period, either P_1 or P_0; columns (4–5) contain the

[1]EPIC 201585823 was described by Kurtz et al. (2016) as a 'rare triple-mode RR Lyrae star'. We find it to be a typical intermediate-metallicity classical RRd star (of the type found in Oosterhoff type I globular clusters) and 'rare' only in the sense that RRd stars in general are relatively rare. The third mode is the very-low-amplitude non-radial mode that appears to be common in RRd stars.

Table 4. Fourier phase-difference parameters, ϕ^s_{21} and ϕ^s_{31}, and amplitude-ratio parameters, R_{21} and R_{31}, for the radial first-overtone pulsations of the 72 classical double-mode RR Lyrae (cRRd) stars observed during the *K2* mission. All are derived from Fourier decomposition of the *K2* photometry and thus are on the *Kp* photometric system. Note that the phase-difference parameters are sine values (which are related to cosine values according to $\phi^c_{21} = \phi^s_{21} + \pi/2$ and $\phi^c_{31} = \phi^s_{31} - \pi$).

EPIC no. (1)	K2 Campaign (2)	P_1 (d) (3)	$\phi^s_{21,1}$(Kp) (radians) (4)	$\phi^s_{31,1}$(Kp) (radians) (5)	$R_{21,1}$(Kp) (6)	$R_{31,1}$(Kp) (7)
060018653	E2	0.4023084(±4)	3.35 ± 0.08	6.33 ± 0.07	0.177 ± 0.014	0.080 ± 0.005
060018662	E2	0.4175081(±3)	3.27 ± 0.08	6.20 ± 0.08	0.230 ± 0.017	0.083 ± 0.005
201585823	C1	0.3594190(±2)	3.26 ± 0.01	6.32 ± 0.01	0.153 ± 0.001	0.065 ± 0.001
210600482	C4	0.362471(±1)	3.38 ± 0.01	6.39 ± 0.02	0.157 ± 0.001	0.058 ± 0.001
210831816	C4	0.3638034(±9)	3.32 ± 0.01	6.65 ± 0.02	0.124 ± 0.001	0.062 ± 0.001
210933539	C4	0.35861619(±2)	3.31 ± 0.01	6.19 ± 0.01	0.171 ± 0.001	0.060 ± 0.001
211072039	C4	0.393491(±2)	3.28 ± 0.01	6.25 ± 0.03	0.181 ± 0.002	0.075 ± 0.002
211694449	C5,18	0.34436220(±4)	3.31 ± 0.01	5.63 ± 0.04	0.193 ± 0.002	0.035 ± 0.001
211888680	C5,16	0.3593838(±1)	3.31 ± 0.01	6.38 ± 0.03	0.155 ± 0.002	0.059 ± 0.002
211898723	C5,18	0.37651088(±4)	3.45 ± 0.01	6.40 ± 0.02	0.162 ± 0.001	0.060 ± 0.001
212335848	C6	0.355068(±2)	3.23 ± 0.01	6.37 ± 0.03	0.145 ± 0.002	0.063 ± 0.002
212449019	C6	0.363388(±1)	3.21 ± 0.01	6.33 ± 0.03	0.144 ± 0.002	0.064 ± 0.002
212455160	C6,17	0.349321(±2)	3.29 ± 0.02	6.27 ± 0.05	0.157 ± 0.003	0.056 ± 0.003
212547473	C6	0.406430(±1)	3.41 ± 0.01	6.39 ± 0.02	0.171 ± 0.001	0.068 ± 0.001
213514736	C7	0.375213(±4)	3.35 ± 0.02	6.13 ± 0.07	0.199 ± 0.004	0.060 ± 0.004
214147122	C7	0.403654(±3)	3.36 ± 0.01	6.41 ± 0.03	0.167 ± 0.002	0.071 ± 0.002
229228175	C7	0.349452(±11)	3.35 ± 0.07	6.77 ± 0.14	0.135 ± 0.010	0.068 ± 0.010
229228184	C7	0.341053(±15)	3.46 ± 0.12	6.38 ± 0.23	0.130 ± 0.015	0.066 ± 0.015
229228194	C7	0.38971(±2)	3.70 ± 0.06	6.67 ± 0.16	0.217 ± 0.004	0.077 ± 0.004
229228220	C7	0.363387(±6)	3.21 ± 0.06	6.36 ± 0.11	0.127 ± 0.007	0.072 ± 0.007
220254937	C8	0.400127(±3)	3.34 ± 0.02	6.33 ± 0.05	0.179 ± 0.003	0.077 ± 0.003
220604574	C8	0.354733(±1)	3.28 ± 0.01	6.59 ± 0.02	0.131 ± 0.001	0.069 ± 0.001
220636134	C8	0.3737393(±7)	3.29 ± 0.01	6.24 ± 0.03	0.175 ± 0.002	0.068 ± 0.002
229228811	C8	0.372911(±2)	3.37 ± 0.01	6.53 ± 0.03	0.145 ± 0.002	0.065 ± 0.002
224366356	C9	0.3430486(±4)	3.13 ± 0.07	5.71 ± 0.23	0.180 ± 0.012	0.053 ± 0.012
223051735	C9	0.4233213(±2)	3.44 ± 0.07	6.21 ± 0.16	0.199 ± 0.014	0.087 ± 0.014
201152424	C10	0.358500(±2)	3.41 ± 0.02	6.82 ± 0.03	0.122 ± 0.002	0.068 ± 0.002
201440678	C10	0.376676(±2)	3.39 ± 0.02	6.62 ± 0.03	0.132 ± 0.002	0.066 ± 0.002
201519136	C10	0.344312(±2)	3.36 ± 0.01	6.25 ± 0.04	0.159 ± 0.002	0.051 ± 0.002
228800773	C10	0.372744(±4)	3.21 ± 0.02	6.13 ± 0.05	0.187 ± 0.004	0.069 ± 0.004
228952519	C10	0.40349(±7)	3.19 ± 0.08	6.03 ± 0.10	0.195 ± 0.015	0.087 ± 0.008
248369176	C10	0.424078(±10)	3.35 ± 0.05	6.34 ± 0.11	0.205 ± 0.009	0.081 ± 0.008
225326517	C11	0.4335412(±2)	3.64 ± 0.02	6.79 ± 0.03	0.149 ± 0.002	0.077 ± 0.002
225456697	C11	0.2943527(±1)	3.08 ± 0.05	6.70 ± 0.09	0.100 ± 0.005	0.049 ± 0.005
235631055	C11	0.4327289(±2)	3.73 ± 0.03	6.73 ± 0.07	0.199 ± 0.005	0.084 ± 0.005
235794591	C11	0.4040492(±1)	3.45 ± 0.02	6.50 ± 0.04	0.190 ± 0.003	0.077 ± 0.003
236212613	C11	0.3489577(±2)	3.33 ± 0.03	6.40 ± 0.08	0.144 ± 0.004	0.059 ± 0.004
251248825	C11	0.4041701(±2)	3.61 ± 0.02	6.81 ± 0.05	0.226 ± 0.004	0.084 ± 0.004
251248826	C11	0.3182948(±2)	3.85 ± 0.04	6.28 ± 0.08	0.141 ± 0.006	0.071 ± 0.006
251248827	C11	0.3379169(±1)	3.74 ± 0.03	6.01 ± 0.13	0.172 ± 0.005	0.034 ± 0.004
251248830	C11	0.310017(±8)	3.68 ± 0.12	6.37 ± 0.51	0.145 ± 0.017	0.033 ± 0.016
245974758	C12	0.3533078(±4)	3.38 ± 0.01	6.32 ± 0.01	0.161 ± 0.001	0.057 ± 0.001
246058914	C12	0.3361100(±4)	3.37 ± 0.01	5.85 ± 0.04	0.171 ± 0.002	0.039 ± 0.001
251456808	C12	0.348582(±9)	3.19 ± 0.09	6.02 ± 0.21	0.175 ± 0.014	0.068 ± 0.014
247334376	C13	0.403243(±9)	3.31 ± 0.05	6.38 ± 0.10	0.193 ± 0.009	0.088 ± 0.008
201749391	C14	0.3573249(±3)	3.31 ± 0.01	6.29 ± 0.01	0.168 ± 0.001	0.063 ± 0.001
248426222	C14	0.401116(±3)	3.32 ± 0.01	6.13 ± 0.02	0.213 ± 0.002	0.077 ± 0.002
248509474	C14	0.4151037(±4)	3.48 ± 0.01	6.27 ± 0.01	0.206 ± 0.001	0.080 ± 0.001
248514834	C14	0.4344186(±2)	3.22 ± 0.01	6.23 ± 0.01	0.250 ± 0.001	0.088 ± 0.001
248653210	C14	0.350434(±2)	3.28 ± 0.02	6.36 ± 0.04	0.143 ± 0.003	0.062 ± 0.003
248653582	C14	0.4027261(±2)	3.34 ± 0.01	6.18 ± 0.01	0.218 ± 0.001	0.081 ± 0.001
248667792	C14	0.358942(±1)	3.26 ± 0.01	6.30 ± 0.02	0.160 ± 0.002	0.064 ± 0.002
248730795	C14	0.390117(±1)	3.26 ± 0.01	6.26 ± 0.02	0.188 ± 0.001	0.076 ± 0.001
248731983	C14	0.4175000(±1)	3.47 ± 0.01	6.39 ± 0.01	0.193 ± 0.001	0.079 ± 0.001
248827979	C14	0.389714(±8)	3.28 ± 0.02	6.00 ± 0.04	0.219 ± 0.003	0.075 ± 0.003
248845745	C14	0.358376(±2)	3.28 ± 0.01	6.51 ± 0.03	0.143 ± 0.002	0.068 ± 0.002
248871792	C14	0.3763140(±2)	3.31 ± 0.01	5.95 ± 0.01	0.213 ± 0.001	0.064 ± 0.001
249790928	C15	0.4306134(±9)	3.80 ± 0.01	7.09 ± 0.01	0.133 ± 0.001	0.072 ± 0.001
250056977	C15	0.3967475(±2)	3.31 ± 0.01	5.93 ± 0.01	0.237 ± 0.001	0.081 ± 0.001

Table 4 – *continued*

EPIC no. (1)	K2 Campaign (2)	P_1 (d) (3)	$\phi^s_{21,1}$(Kp) (radians) (4)	$\phi^s_{31,1}$(Kp) (radians) (5)	$R_{21,1}$(Kp) (6)	$R_{31,1}$(Kp) (7)
211665293	C16	0.366065(±1)	3.37 ± 0.01	6.59 ± 0.02	0.135 ± 0.001	0.064 ± 0.001
212467099	C17	0.386354(±3)	3.24 ± 0.01	6.22 ± 0.03	0.186 ± 0.002	0.078 ± 0.002
212498188	C17	0.371357(±2)	3.30 ± 0.01	6.00 ± 0.03	0.202 ± 0.002	0.061 ± 0.002
212615778	C17	0.348889(±1)	3.40 ± 0.01	6.20 ± 0.03	0.166 ± 0.001	0.049 ± 0.001
212819285	C17	0.353446(±4)	3.30 ± 0.03	6.36 ± 0.07	0.152 ± 0.004	0.059 ± 0.004
251521080	C17	0.373014(±5)	3.24 ± 0.03	6.21 ± 0.07	0.164 ± 0.005	0.064 ± 0.005
251629085	C17	0.344183(±4)	3.19 ± 0.04	6.77 ± 0.06	0.105 ± 0.004	0.065 ± 0.004
251809772	C17	0.355035(±3)	3.30 ± 0.02	6.13 ± 0.05	0.167 ± 0.003	0.057 ± 0.003
251809814	C17	0.347284(±3)	3.41 ± 0.02	6.28 ± 0.06	0.160 ± 0.003	0.050 ± 0.003
251809825	C17	0.353727(±3)	3.38 ± 0.02	6.39 ± 0.06	0.153 ± 0.004	0.059 ± 0.004
251809832	C17	0.387565(±5)	3.23 ± 0.03	6.25 ± 0.06	0.184 ± 0.005	0.082 ± 0.005
251809860	C17	0.363480(±8)	3.38 ± 0.05	6.48 ± 0.17	0.181 ± 0.009	0.052 ± 0.009
251809870	C17	0.375881(±14)	3.07 ± 0.09	6.06 ± 0.23	0.201 ± 0.017	0.074 ± 0.017
mean ± s.e.			3.36 ± 0.02	6.33 ± 0.03	0.171 ± 0.004	0.067 ± 0.001

corresponding phase-difference parameters, $\phi^s_{21}(=\phi^s_2 - 2\phi^s_1)$ and $\phi^s_{31}(=\phi^s_3 - 3\phi^s_1)$, where the 's' superscripts indicate that the Fourier fits to the *Kepler/K2* photometry are based on sine functions (and not cosine functions, as is the case for the OGLE survey); and columns (6–7) contain the amplitude-ratio parameters, $R_{21}(=A_2/A_1)$ and $R_{31}(=A_3/A_1)$. Mean values (± standard errors of the mean) are given at the bottom of each column.

The precision of the derived Fourier parameters is very high for both pulsation modes. For the first-overtone pulsations (see Table 4) the uncertainties in ϕ^s_{21} and ϕ^s_{31} typically are ∼0.02 and ∼0.04 radians, respectively, and for R_{21} and R_{31} the uncertainties are ∼0.002. For the fundamental-mode pulsations (see Table 5), which are usually of lower amplitude, the uncertainties are larger, ∼0.04 and ∼0.26 radians for ϕ^s_{21} and ϕ^s_{31}, respectively, and ∼0.005 for both R_{21} and R_{31}. Differences in the uncertainties for individual stars are due to the non-homogeneous nature of the sample, which is drawn from Ecliptic Plane and Galactic Bulge fields having different star densities, and other factors such as the methods used to produce the detrended and outlier-free photometry. Owing to the low amplitudes of the non-radial pulsations their inclusion in the fitted model (equation 3) was found to have little effect on the derived Fourier decomposition parameters for the radial pulsations.

4 DISCUSSION

The pulsation properties of RRd stars are determined by their masses, luminosities, effective temperatures, metal abundances, and other physical characteristics. Analysis of correlations among descriptors of the observed light curve, such as the periods, amplitudes, and Fourier parameters, are key to making inferences about the unknown physical quantities that drive the oscillations. In Section 4.1 within-mode and between-mode correlations among 12 pulsation descriptors are given for the *K2* cRRd stars. The strongest correlation is between the fundamental and first overtone periods. In Section 4.2 this correlation is discussed within the framework of a simple statistical model that explains both the observed P_1 versus P_0 and Petersen diagrams. Dependencies of the pulsation amplitudes and several Fourier parameters on period are discussed in Section 4.3. In Section 4.4 an independent sample of RRd stars with spectroscopic metal abundances and known periods is used to derive a period-[Fe/H] calibration equation consistent with the P_1–P_0 correlation results in Section 4.2. The equation is used to estimate metal abundances for the cRRd stars observed by *K2* and for 2130 cRRd stars observed by the *Gaia* Mission. The effect of misclassification bias on the estimated [Fe/H] values is also discussed.

4.1 Within- and between-mode correlations

For RRd and other multimode pulsators two kinds of correlations are of interest: *cross-mode* and *within-mode*. Examples of the former include the correlations between P_1 and P_0, and between A_1 and A_0 (see figs 5a,b of NM21), and examples of the latter include the period–amplitude relations for each of the two radial modes (see Fig. 6 below). For single-mode RRab and RRc stars correlations are necessarily within-mode correlations. Pearson correlation coefficients involving 12 descriptors of the light curves are presented for the 72 *K2* cRRd stars in Table 6. In the top section all pairwise correlations (and *p*-values measuring statistical significance) are given for the P_1, A_1, R_{21}, R_{31}, ϕ_{21}, and ϕ_{31} parameter estimates for the first-overtone mode; the middle section gives the corresponding correlations for the fundamental mode; and cross-mode correlation coefficients are given in the bottom section.

Not surprisingly, the strongest correlation is the cross-correlation between P_0 and P_1 (bottom right corner of Table 6), with $r = 0.9999$ and $p<0.001$. There is also evidence that A_1 and A_0 and all but one of the four Fourier parameters (ϕ_{31}) are cross-correlated for the two modes ($p\leq0.02$), where $r > 0$ (i.e. the correlation is positive) in all cases except R_{31} (diagonal entries, Table 6c). Patterns of within-mode correlation differ for the first-overtone and fundamental modes. For instance, the Fourier parameters R_{21} and R_{31} are strongly correlated with period for the first-overtone (Table 6a), but not for the fundamental mode; whereas, amplitude is strongly and negatively correlated with period for the fundamental mode (Table 6b) but shows no significant correlation with period in the first-overtone case. The nature of these correlations and their implications are discussed below.

4.2 P_0, P_1 relationships

Theoretical pulsation models imply that the strong correlation between P_0 and P_1 arises because both periods depend on the same unobserved physical factors: mass, luminosity, temperature, [Fe/H],

Table 5. Fourier parameters for the radial fundamental mode pulsations. (See Table 4 for column descriptions).

EPIC no. (1)	K2 Campaign (2)	P_0 (d) (3)	$\phi^s_{21,0}$(Kp) (radians) (4)	$\phi^s_{31,0}$(Kp) (radians) (5)	$R_{21,0}$(Kp) (6)	$R_{31,0}$(Kp) (7)
060018653	E2	0.539441(±1)	2.35 ± 0.16	4.68 ± 0.63	0.104 ± 0.014	0.022 ± 0.014
060018662	E2	0.559323(±1)	2.23 ± 0.11	4.52 ± 0.57	0.096 ± 0.011	0.017 ± 0.010
201585823	C1	0.4825903(±6)	2.32 ± 0.01	5.32 ± 0.03	0.125 ± 0.001	0.015 ± 0.001
210600482	C4	0.487191(±3)	2.39 ± 0.01	5.48 ± 0.10	0.165 ± 0.002	0.022 ± 0.002
210831816	C4	0.488793(±6)	2.45 ± 0.06	5.3 ± 1.4	0.063 ± 0.004	0.003 ± 0.004
210933539	C4	0.4818008(±5)	2.37 ± 0.01	5.33 ± 0.01	0.177 ± 0.001	0.031 ± 0.001
211072039	C4	0.527041(±11)	2.26 ± 0.08	5.78 ± 0.63	0.092 ± 0.007	0.011 ± 0.007
211694449	C5,18	0.46365024(±6)	2.35 ± 0.01	5.27 ± 0.02	0.258 ± 0.001	0.068 ± 0.001
211888680	C5,16	0.4829926(±2)	2.37 ± 0.02	5.58 ± 0.13	0.152 ± 0.003	0.023 ± 0.003
211898723	C5,18	0.5058274(±1)	2.40 ± 0.01	5.55 ± 0.06	0.176 ± 0.002	0.024 ± 0.001
212335848	C6	0.476856(±6)	2.32 ± 0.04	5.33 ± 0.43	0.111 ± 0.004	0.010 ± 0.004
212449019	C6	0.487778(±6)	2.38 ± 0.04	5.70 ± 0.38	0.113 ± 0.004	0.011 ± 0.004
212455160	C6,17	0.469592(±4)	2.32 ± 0.03	5.28 ± 0.20	0.168 ± 0.004	0.022 ± 0.004
212547473	C6	0.545079(±4)	2.37 ± 0.02	5.59 ± 0.12	0.125 ± 0.002	0.018 ± 0.002
213514736	C7	0.503583(±9)	2.35 ± 0.03	5.37 ± 0.17	0.193 ± 0.006	0.035 ± 0.006
214147122	C7	0.541040(±14)	2.44 ± 0.19	4.48 ± 0.35	0.083 ± 0.015	0.044 ± 0.015
229228175	C7	0.46954(±5)	2.85 ± 0.30	...	0.131 ± 0.038	...
229228184	C7	0.45943(±4)	2.59 ± 0.11	5.53 ± 0.31	0.204 ± 0.021	0.067 ± 0.020
229228194	C7	0.52263(±10)	2.70 ± 0.11	5.7 ± 1.2	0.168 ± 0.006	0.015 ± 0.006
229228220	C7	0.48774(±3)	...	4.46 ± 0.77	0.055 ± 0.029	0.037 ± 0.029
220254937	C8	0.535934(±17)	2.42 ± 0.11	6.1 ± 2.2	0.101 ± 0.011	0.005 ± 0.011
220604574	C8	0.476772(±7)	2.44 ± 0.07	5.33 ± 0.39	0.071 ± 0.005	0.012 ± 0.005
220636134	C8	0.501375(±2)	2.27 ± 0.03	5.37 ± 0.22	0.134 ± 0.004	0.018 ± 0.004
229228811	C8	0.500219(±6)	2.30 ± 0.04	5.38 ± 0.36	0.121 ± 0.004	0.012 ± 0.004
224366356	C9	0.4619359(±6)	2.35 ± 0.06	5.01 ± 0.17	0.244 ± 0.013	0.077 ± 0.013
223051735	C9	0.5677371(±7)	2.66 ± 0.13	6.0 ± 1.0	0.252 ± 0.029	0.028 ± 0.028
201152424	C10	0.481725(±9)	2.47 ± 0.14	...	0.052 ± 0.007	0.017 ± 0.007
201440678	C10	0.505614(±11)	2.37 ± 0.07	5.0 ± 1.1	0.083 ± 0.006	0.006 ± 0.006
201519136	C10	0.463376(±4)	2.37 ± 0.01	5.24 ± 0.07	0.190 ± 0.002	0.033 ± 0.002
228800773	C10	0.49988(±1)	2.27 ± 0.05	5.51 ± 0.34	0.149 ± 0.007	0.019 ± 0.007
228952519	C10	0.5406(±15)	...	...	0.026 ± 0.026	0.020 ± 0.026
248369176	C10	0.56828(±3)	2.20 ± 0.14	5.97 ± 0.84	0.146 ± 0.020	0.024 ± 0.020
225326517	C11	0.581816(±1)	2.52 ± 0.16	6.70 ± 0.74	0.059 ± 0.010	0.013 ± 0.010
225456697	C11	0.3998380(±4)	2.52 ± 0.07	5.06 ± 0.53	0.136 ± 0.009	0.016 ± 0.009
235631055	C11	0.5804633(±7)	2.51 ± 0.10	5.53 ± 0.45	0.121 ± 0.012	0.027 ± 0.012
235794591	C11	0.5415829(±5)	2.34 ± 0.10	4.71 ± 0.22	0.090 ± 0.009	0.040 ± 0.009
236212613	C11	0.4692002(±4)	2.40 ± 0.05	6.02 ± 0.33	0.143 ± 0.007	0.022 ± 0.007
251248825	C11	0.5413433(±9)	2.11 ± 0.23	6.1 ± 1.0	0.066 ± 0.015	0.015 ± 0.015
251248826	C11	0.430234(±1)	2.32 ± 0.49	...	0.044 ± 0.021	0.009 ± 0.021
251248827	C11	0.4552683(±2)	2.64 ± 0.02	5.63 ± 0.11	0.212 ± 0.005	0.044 ± 0.005
251248830	C11	0.419592(±14)	2.67 ± 0.08	5.16 ± 0.48	0.209 ± 0.016	0.037 ± 0.016
245974758	C12	0.475291(±5)	2.37 ± 0.01	5.42 ± 0.03	0.185 ± 0.001	0.030 ± 0.001
246058914	C12	0.4529476(±7)	2.37 ± 0.01	5.25 ± 0.03	0.240 ± 0.001	0.055 ± 0.001
251456808	C12	0.46898(±2)	2.31 ± 0.10	5.53 ± 0.74	0.188 ± 0.018	0.024 ± 0.018
247334376	C13	0.53958(±4)	...	...	0.037 ± 0.053	...
201749391	C14	0.479930(±1)	2.35 ± 0.01	5.29 ± 0.02	0.162 ± 0.001	0.023 ± 0.001
248426222	C14	0.537644(±8)	2.34 ± 0.02	5.46 ± 0.12	0.143 ± 0.003	0.025 ± 0.003
248509474	C14	0.557312(±1)	2.44 ± 0.01	5.65 ± 0.02	0.179 ± 0.001	0.029 ± 0.001
248514834	C14	0.581287(±2)	2.35 ± 0.01	5.60 ± 0.11	0.064 ± 0.001	0.006 ± 0.001
248653210	C14	0.471007(±6)	2.30 ± 0.04	5.47 ± 0.23	0.143 ± 0.005	0.021 ± 0.005
248653582	C14	0.5398778(±5)	2.36 ± 0.01	5.57 ± 0.01	0.142 ± 0.001	0.023 ± 0.001
248667792	C14	0.482054(±4)	2.32 ± 0.02	5.46 ± 0.15	0.138 ± 0.003	0.018 ± 0.003
248730795	C14	0.522545(±6)	2.29 ± 0.04	5.40 ± 0.31	0.094 ± 0.004	0.012 ± 0.004
248731983	C14	0.5600838(±5)	2.42 ± 0.01	5.63 ± 0.02	0.135 ± 0.001	0.017 ± 0.001
248827979	C14	0.522807(±10)	2.33 ± 0.03	5.36 ± 0.15	0.179 ± 0.005	0.033 ± 0.005
248845745	C14	0.481123(±8)	2.47 ± 0.07	4.55 ± 0.62	0.092 ± 0.006	0.010 ± 0.006
248871792	C14	0.5054967(±4)	2.33 ± 0.01	5.40 ± 0.01	0.211 ± 0.001	0.047 ± 0.001
249790928	C15	0.578550(±6)	2.59 ± 0.05	5.84 ± 0.86	0.066 ± 0.003	0.004 ± 0.003
250056977	C15	0.532603(±1)	2.39 ± 0.01	5.52 ± 0.01	0.203 ± 0.001	0.047 ± 0.001
211665293	C16	0.491516(±4)	2.38 ± 0.03	5.51 ± 0.48	0.093 ± 0.003	0.006 ± 0.003
212467099	C17	0.517170(±18)	2.36 ± 0.13	...	0.073 ± 0.010	0.004 ± 0.010
212498188	C17	0.498643(±4)	2.34 ± 0.01	5.41 ± 0.05	0.207 ± 0.002	0.045 ± 0.002

Table 5 – *continued*

EPIC no. (1)	K2 Campaign (2)	P_0 (d) (3)	$\phi^s_{21,0}$(Kp) (radians) (4)	$\phi^s_{31,0}$(Kp) (radians) (5)	$R_{21,0}$(Kp) (6)	$R_{31,0}$(Kp) (7)
212615778	C17	0.469391(±2)	2.37 ± 0.01	5.38 ± 0.04	0.196 ± 0.002	0.037 ± 0.002
212819285	C17	0.474968(±13)	2.29 ± 0.06	6.14 ± 0.51	0.131 ± 0.008	0.016 ± 0.008
251521080	C17	0.50087(±2)	2.41 ± 0.04	5.34 ± 0.26	0.172 ± 0.007	0.027 ± 0.007
251629085	C17	0.46311(±4)	...	5.1 ± 1.1	0.043 ± 0.024	0.023 ± 0.024
251809772	C17	0.477332(±6)	2.28 ± 0.02	5.51 ± 0.14	0.186 ± 0.004	0.030 ± 0.004
251809814	C17	0.467124(±6)	2.38 ± 0.03	5.33 ± 0.12	0.170 ± 0.004	0.033 ± 0.004
251809825	C17	0.475900(±8)	2.41 ± 0.03	5.42 ± 0.20	0.171 ± 0.005	0.025 ± 0.005
251809832	C17	0.51919(±3)	2.52 ± 0.32	...	0.067 ± 0.021	0.043 ± 0.021
251809860	C17	0.488442(±19)	2.34 ± 0.07	5.2 ± 1.8	0.181 ± 0.012	0.007 ± 0.012
251809870	C17	0.50483(±3)	2.21 ± 0.09	4.99 ± 0.39	0.235 ± 0.019	0.048 ± 0.019
mean ± s.e.			2.39 ± 0.02	5.41 ± 0.05	0.141 ± 0.007	0.025 ± 0.002

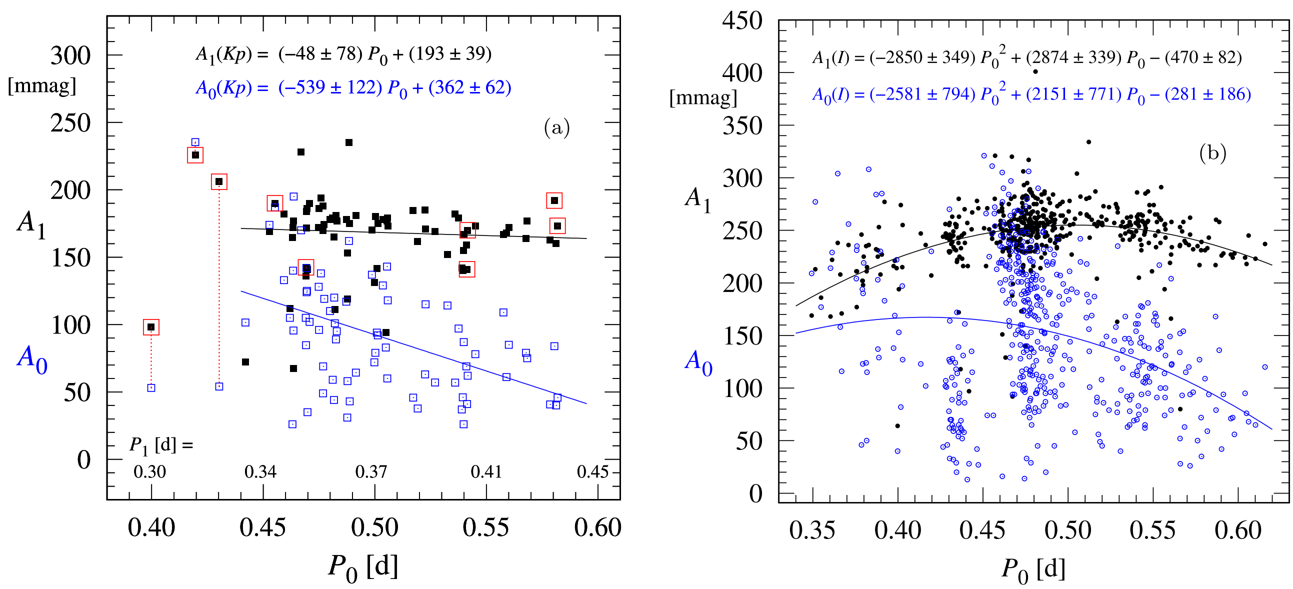

Figure 6. Period–amplitude (*P*–*A*) diagrams for both radial pulsation modes of the cRRd stars observed by *K2* (left) and by OGLE (right). (a) For the *K2* stars the first-overtone amplitudes, $A_1(Kp)$ (solid squares), and the fundamental mode amplitudes $A_0(Kp)$ (open boxes), are Fourier first-term values. Large boxes surround the points representing the first-overtone components of the Campaign 11 stars. (b) For the OGLE stars the $A_1(I)$ (solid dots) and $A_0(I)$ (open circles) amplitudes are trough-to-peak (min-to-max) values derived from *I*-passband photometry.

etc. Consider the following statistical model[2] that embodies this idea:

$$\sqrt{P_0} = a_0 + b_0 X + \epsilon_0$$
$$\sqrt{P_1} = a_1 + b_1 X + \epsilon_1, \qquad (2)$$

where the observed periods are assumed to depend primarily on a single common (unmeasured or unknown) factor *X*. (The special case where X = [Fe/H] is discussed in Section 4.4.2). The square-root transformation is applied to the periods to ensure that the functional forms of the P_1–P_0 and the P_1/P_0 versus P_0 relationships are consistent with the observations – see the discussion that follows.

[2]Models that express the correlation structure of a set of observable variables in terms of a system of linear equations involving a smaller number of unobserved 'common factors' are known as 'factor analysis' models in the statistical literature. Equation (2) has only two observable variables (P_0 and P_1) and one common factor (X) but the model can easily be generalized to include additional observable variables (e.g. A_0 and A_1) and more than one common factor. See Morrison (1976).

Assume that *X* has a normal distribution with mean 0 and variance 1 (if necessary, replace X with $\frac{X-<X>}{\sqrt{\mathrm{var}X}}$), and that the measurement errors in $\sqrt{P_0}$ and $\sqrt{P_1}$, ϵ_0 and ϵ_1, are independent normally distributed random variables with mean 0 and respective variances σ_0^2 and σ_1^2.

It follows from equation (2) that $(\sqrt{P_0}, \sqrt{P_1})^T$ has a bivariate normal distribution with mean $(a_0, a_1)^T$, variance–covariance matrix

$$\begin{bmatrix} b_0^2 + \sigma_0^2 & b_0\, b_1 \\ b_0\, b_1 & b_1^2 + \sigma_1^2 \end{bmatrix},$$

and correlation coefficient

$$\rho = \frac{b_0 b_1}{\sqrt{(b_0^2 + \sigma_0^2) \times (b_1^2 + \sigma_1^2)}}.$$

Notice that if σ_0^2 and σ_1^2 are small compared with b_0^2 and b_1^2 then ρ is close to 1.

It also follows from the properties of the bivariate normal distribution (see Hogg & Craig 1959) that the conditional mean and variance of $\sqrt{P_1}$ given $\sqrt{P_0}$ are:

Table 6. Pearson correlation coefficients (r) and their associated p-values (in *italics*) for the 72 *K2* cRRd stars (Tables 4–5). The correlation coefficient is a measure of the linear association between the respective row and column variables, and r^2 is the proportion of variability in the row (column) variable that is explained by the column (row) variable, where a positive (negative) value corresponds to a positive (negative) slope. Small p-values (<0.05) correspond to statistically significant (linear) correlation. If $p < 0.01$ the correlation coefficients are highlighted in boldface. Note that Sections (a) and (b) are symmetric about the diagonal.

	$\phi_{21,1}$	$\phi_{31,1}$	$R_{21,1}$	$R_{31,1}$	A_1	P_1
	(a) First-overtone correlations					
$\phi_{21,1}$	1.00	**0.36**	−0.05	−0.06	**0.48**	0.16
	...	*0.002*	*0.69*	*0.64*	*<0.001*	*0.19*
$\phi_{31,1}$	**0.36**	1.00	**−0.54**	0.21	0.12	0.13
	0.002	...	*<0.001*	*0.08*	*0.34*	*0.27*
$R_{21,1}$	−0.05	**−0.54**	1.00	**0.45**	−0.06	**0.61**
	0.69	*<0.001*	...	*<0.001*	*0.60*	<0.001
$R_{31,1}$	−0.06	0.21	**0.45**	1.00	−0.25	**0.80**
	0.64	*0.08*	*<0.001*	...	*0.04*	<0.001
A_1	**0.48**	0.12	−0.06	−0.25	1.00	−0.08
	0.001	*0.34*	*0.60*	*0.04*	...	*0.93*
P_1	0.16	0.13	**0.61**	**0.80**	−0.08	1.00
	0.19	*0.27*	*<0.001*	*<0.001*	*0.93*	...
	$\phi_{21,0}$	$\phi_{31,0}$	$R_{21,0}$	$R_{31,0}$	A_0	P_0
	(b) Fundamental-mode correlations					
$\phi_{21,0}$	1.00	0.08	0.05	0.13	0.06	−0.11
	...	*0.53*	*0.68*	*0.29*	*0.64*	*0.38*
$\phi_{31,0}$	0.08	1.00	0.02	−0.26	−0.02	0.27
	0.53	...	*0.85*	*0.04*	*0.88*	*0.03*
$R_{21,0}$	0.05	0.02	1.00	**0.68**	**0.82**	−0.28
	0.68	*0.85*	...	*<0.001*	*<0.001*	*0.02*
$R_{31,0}$	0.13	−0.26	**0.68**	1.00	**0.55**	−0.22
	0.29	*0.04*	*<0.001*	...	*<0.001*	*0.07*
A_0	0.06	−0.02	**0.82**	**0.55**	1.00	**−0.43**
	0.64	*0.88*	*<0.001*	*<0.001*	...	*0.002*
P_0	−0.11	0.27	−0.28	−0.22	**−0.43**	1.00
	0.38	*0.03*	*0.02*	*0.07*	*0.002*	...
	$\phi_{21,1}$	$\phi_{31,1}$	$R_{21,1}$	$R_{31,1}$	A_1	P_1
	(c) Cross correlations: Fund. (rows) × 1st Overtone (columns)					
$\phi_{21,0}$	**0.37**	**0.32**	**−0.39**	−0.16	0.08	−0.11
	0.002	*<0.01*	*0.001*	*0.20*	*0.50*	*0.35*
$\phi_{31,0}$	**0.36**	0.15	0.11	0.14	0.18	0.27
	0.004	*0.24*	*0.38*	*0.26*	*0.17*	*0.03*
$R_{21,0}$	−0.10	**−0.68**	0.29	**−0.50**	−0.03	−0.28
	0.41	*<0.001*	*0.02*	*<0.001*	*0.81*	*0.02*
$R_{31,0}$	−0.08	**−0.62**	0.23	**−0.34**	−0.22	−0.23
	0.52	*<0.001*	*0.06*	*0.004*	*0.07*	*0.06*
A_0	0.19	**−0.51**	0.12	**−0.74**	**0.41**	**−0.37**
	0.10	*<0.001*	*0.33*	*<0.001*	*<0.001*	*0.001*
P_0	0.16	0.14	**0.61**	**0.79**	−0.01	**0.9999**
	0.17	*0.26*	*<0.001*	*<0.001*	*0.92*	*<0.001*

$$E\left(\sqrt{P_1}\,\middle|\,\sqrt{P_0}\right) = \left(a_0 - \frac{b_0}{b_1}a_1\right) + \frac{b_0}{b_1}\sqrt{P_0}$$
$$\mathrm{Var}\left(\sqrt{P_1}\,\middle|\,\sqrt{P_0}\right) = \sigma_0^2 + \left(\frac{b_0}{b_1}\right)^2\sigma_1^2,$$

which imply (by the definition of variance) that

$$E\left(P_1\,\middle|\,\sqrt{P_0}\right) = \mathrm{Var}\left(\sqrt{P_1}\,\middle|\,\sqrt{P_0}\right) + \left[E\left(\sqrt{P_1}\,\middle|\,\sqrt{P_0}\right)\right]^2.$$

Since conditioning on $\sqrt{P_0}$ is equivalent to conditioning on P_0 (because P_0 is positive), substitution into the preceding equation gives the conditional mean of P_1 given P_0:

$$E\left(P_1\,\middle|\,P_0\right) = a + b\sqrt{P_0} + cP_0, \qquad (3)$$

where

$$a = \sigma_0^2 + \left(\frac{b_0}{b_1}\right)^2\sigma_1^2 + \left(a_0 - \frac{b_0}{b_1}a_1\right)^2,$$
$$b = 2\,\frac{b_0}{b_1}\left(a_0 - \frac{b_0}{b_1}a_1\right),$$
$$\text{and} \quad c = \left(\frac{b_0}{b_1}\right)^2.$$

Dividing both sides of equation (3) by P_0 gives the conditional mean of the ratio

$$E\left(\frac{P_1}{P_0}\,\middle|\,P_0\right) = \frac{a}{P_0} + \frac{b}{\sqrt{P_0}} + c. \qquad (4)$$

Thus the equation (2) model implies that the expected P_1–P_0 and P_1/P_0 versus P_0 (Petersen diagram) relationships have specific functional forms (given by equations 3 and 4), which can be compared with observations in order to help validate the model or rule out competing models. For example, if $\sqrt{P_0}$ and $\sqrt{P_1}$ in equation (2) are replaced with P_0 and P_1 then

$$E\left(\frac{P_1}{P_0}\,\middle|\,P_0\right) = \frac{a'}{P_0} + b', \qquad (5)$$

which fails to fit the observed Petersen curve for cRRd stars (see the red dotted curve in Fig. 10c, and Section 4.4.2 below).

4.3 Dependencies of amplitudes and Fourier parameters on period

Period–amplitude diagrams have proved useful for distinguishing single-mode RRab and RRc stars. The earliest studies revealed that the metal abundances of RR Lyrae stars correlate with period and amplitude (Oosterhoff 1939; Arp 1955; Preston 1959). More recently, *P–A* relationships and relationships involving Fourier decomposition parameters, such as the period-ϕ_{31} diagram, have been used to infer [Fe/H] for single-mode RRab and RRc stars (e.g. Simon 1990; Kovács & Jurcsik 1996; Sandage 2004; Morgan, Wahl & Wieckhorst 2007; Nemec et al. 2013; Clementini et al. 2023). At a given amplitude (or ϕ_{31}) stars of longer period tend to have higher masses, greater luminosities, and lower metal abundances (see also the hydrodynamical models presented in figs 14 and 15 of Nemec et al. 2011). The *P-A*, *P-*R_{21}, *P-*ϕ_{31}, etc., relationships for the individual modes have not previously been analysed in detail.

4.3.1 *Period–amplitude diagram for cRRd stars*

In Fig. 6 period–amplitude diagrams are plotted for the individual radial pulsation modes for the *K2* cRRd stars (left) and for the 458 OGLE-IV Galactic Disk and Bulge cRRd stars identified by Soszyński et al. (2019). For the *K2* stars the Fourier first-term amplitudes (Table 3) are plotted. For each mode the equation of the least-squares fitted line is given at the top of the graph. Excluded from the fits are the three short-period Galactic Bulge stars observed during Campaign 11 (the two modes of which are connected by red vertical dotted lines). The first-overtone amplitudes A_1 (solid black squares and black line) show a slight, but statistically insignificant, decrease with period, while the usually smaller fundamental mode amplitudes A_0 (open blue boxes and blue line) show a pronounced, statistically significant, decrease with period (see Table 6a,b). As a result the amplitude ratios A_1/A_0 for the cRRd stars with P_0

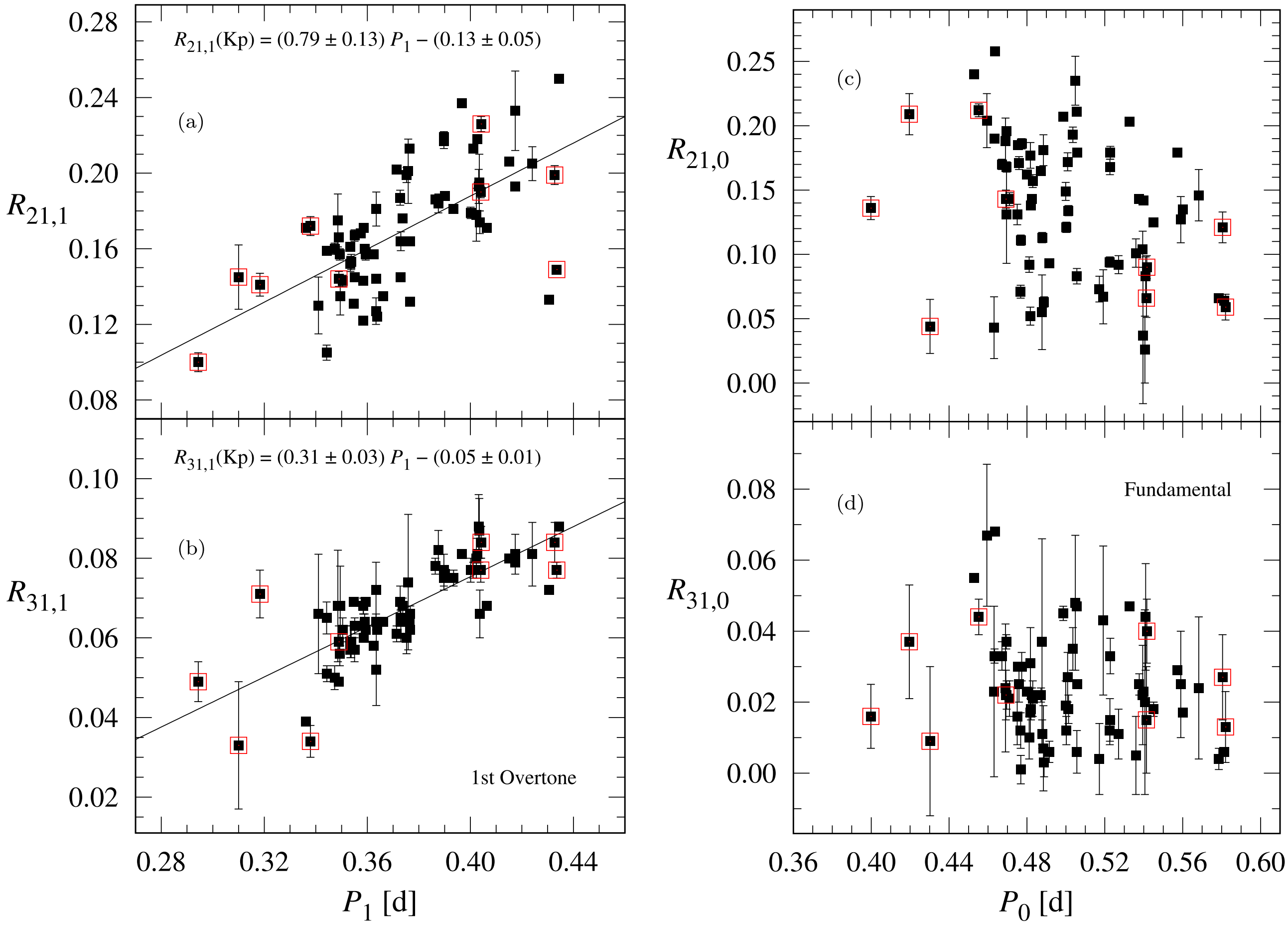

Figure 7. Fourier amplitude-ratio parameters versus period for the 72 Ecliptic Plane and Galactic Bulge cRRd stars observed by *K2*, derived from decomposition of the *Kp*-passband light curves (see Tables 4 and 5). The left panels show the radial first-overtone parameters versus P_1, and the right panels show the fundamental-mode parameters versus P_0. The first-overtone graphs also show least-squares fitted lines and their equations. Correlation coefficients for all four panels can be found in Table 6. The points enclosed by red boxes identify the nine Campaign 11 (Galactic Bulge) cRRd stars.

> 0.44 d (see Fig. 2) increase with increasing period. It follows that intermediate-metallicity (Oosterhoff type I) cRRd stars, which have fundamental mode periods P_0 between 0.45 and 0.51 d, tend to have lower A_1/A_0 ratios than more metal-poor (Oosterhoff type II) cRRd stars which have P_0 between 0.51 and 0.62 d. It is noteworthy that the pronounced downward trend for the fundamental-mode amplitudes (Fig. 6), and the much shallower downward trend for the first-overtone amplitudes, are consistent with the well-known *P*-*A* downward trends for single-mode RRab and RRc stars (see for example, fig. 3 of Soszyński et al. 2009).

The period–amplitude diagram for the two radial pulsation modes of the 458 Galactic Disc and Bulge stars observed by OGLE-IV is plotted in Fig. 6(b). Unlike the *K2* amplitudes, which are Fourier first-term values derived from *Kp* photometry, the OGLE amplitudes are min-to-max values through the *I* filter and thus tend to be larger. Another difference is the presence in the OGLE sample of many cRRd stars with fundamental-mode periods shorter than 0.45 d. Inclusion of these (presumably metal-rich) stars suggests that the fundamental and first-overtone relationships between amplitude and period are non-linear over this broader range of periods. Fitted polynomials, the equations of which are given at the top of the graph, are plotted for the two modes. The period at which the fitted first-overtone amplitude reaches a maximum appears to occur at $P_0 \sim 0.50$ d. For the period range where Figs 6(a) and (b) overlap (i.e. $P_0 > 0.45$ d) both samples show approximately linear downward trends. For periods shorter than 0.42 d the fundamental-mode amplitudes exhibit a large scatter that cannot be explained by period alone. Consequently the large scatter in both graphs, the confounding effect of different filters, and the small range of the period overlap, makes it difficult to establish the precise functional forms of the relationships.

4.3.2 Dependence of Fourier parameters on period

In addition to amplitudes, the Fourier amplitude-ratio and phase-difference parameters (i.e. R_{21}, R_{31}, ϕ^s_{21}, and ϕ^s_{31}) have been used to describe the light curves of pulsating stars and as predictors of the metal abundance of single-mode RR Lyrae stars. Thus it is instructive to examine how these four descriptors correlate with period for cRRd stars. The four panels of Fig. 7 show, for each of the two pulsation components, the R_{21} and R_{31} values for the *K2* cRRd stars plotted against the corresponding pulsation period. The first-overtone graphs (left) show fitted least-squares lines, the equations of which are given in each panel. Since the *K2* survey covers 20 different fields around the Ecliptic Plane the fitted lines describe only overall trends for the composite sample. As expected the R_{21} values (upper panels) are larger than the R_{31} values (lower panels) for both modes. Note

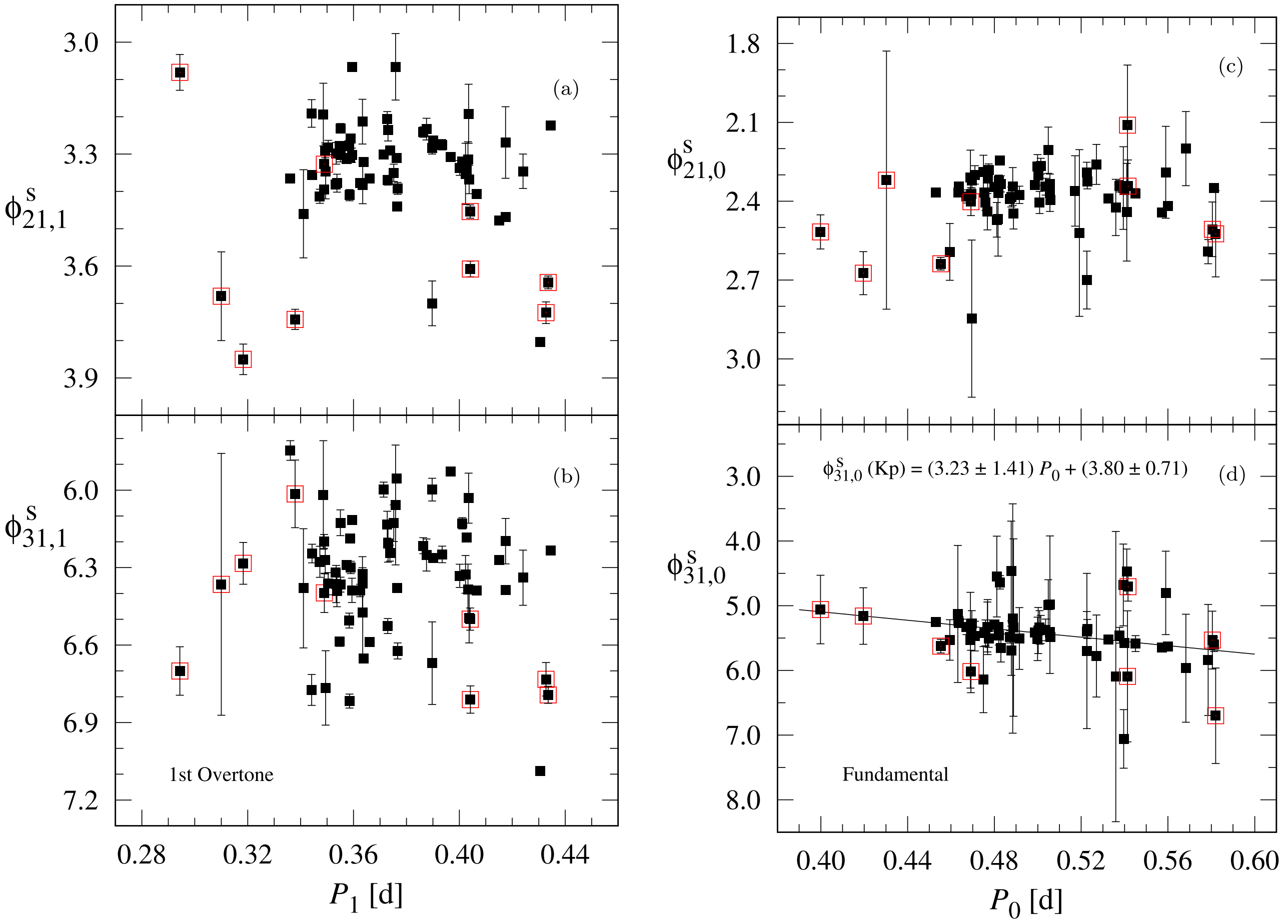

Figure 8. Fourier phase-difference parameters versus period for the first-overtone (left) and fundamental (right) pulsation modes of the cRRd stars observed by *K2*, where the symbols and panels correspond to the amplitude-ratio graphs plotted in Fig. 7.

also that the slopes of the first-overtone lines are positive (Figs 7a and b) and the correlation coefficients for both $R_{21,1}$ and $R_{31,1}$ are highly significant (Table 6a), although the $R_{31,1}$ correlation with P_1 is stronger. There is no evidence of such a clear positive trend in the $R_{21,1}$ versus $\log P_0$ graph for the first overtone of 986 RRd stars in the Large Magellanic Cloud observed by the OGLE survey (fig. 2 of Soszyński et al. 2009). The dependence of $R_{21,0}$ and $R_{31,0}$ on period is less clear for the fundamental mode (Figs 7c and d). There is some evidence that both ratios are negatively correlated with P_0 (Table 6b) but evidence for a simple linear relationship is lacking.

Graphs of the Fourier phase-difference parameters ϕ^{s}_{21} and ϕ^{s}_{31} versus pulsation period are given in Fig. 8. The layout and symbols match those seen in Fig. 7. Only $\phi^{s}_{31,0}$ shows a statistically significant correlation with period (Table 6b); the fitted least-squares line and its equation are shown in panel (d). Note that because the phase-differences are plotted on a reversed scale (see fig. 3 of Sandage 2004; and figs 4 and 12 of Nemec et al. 2013) the line appears to slope downwards, even though the correlation is positive.

4.3.3 Amplitudes, amplitude ratios, and periods

In Fig. 9 Fourier amplitudes and amplitude-ratio parameters are compared for the two pulsation modes. The first-overtone amplitude A_1 is plotted against the fundamental-mode amplitude A_0 in the upper left panel (Fig. 9a), and the first-overtone amplitude-ratio parameter $R_{21,1}$ is plotted against its fundamental-mode counterpart $R_{21,0}$ in the upper right panel (Fig. 9c). The lower panels show the corresponding ratios versus A_0 (Fig. 9b) and versus $R_{21,0}$ (Fig. 9d). The amplitudes are the *Kp* values given in Table 3, and the R_{21} values are given in Tables 4 and 5. Three period groups are plotted with different symbols: $P_0 > 0.51$ d (blue open circles); $0.45 < P_0 < 0.51$ d (black squares); and $P_0 < 0.45$ d (red open triangles).

The *K2* stars in Fig. 9(a) appear to separate into three amplitude groups, which are also evident in a histogram (not shown) of the A_1 values. Fifty-three of the 72 stars form a horizontal band with $155 < A_1 < 200$ mmag, where $< A_1 > = 175 \pm 2$ mmag and $< A_0 > = 90$ mmag. A second group of 15 stars ($A_1 < 155$ mmag) lies below this band, where $< A_1 > = 130 \pm 3$ mmag and $< A_0 > = 70$ mmag, and five stars lie above the band ($A_1 > 200$ mmag) with $< A_1 > = 224 \pm 6$ mmag and $< A_0 > = 160$ mmag. The mean A_1 values for the three amplitude groups are indicated by horizontal lines. The positive Pearson correlation coefficient (Table 6c) reflects the increase in $< A_1 >$ as $< A_0 >$ increases. A similar pattern is seen for the 458 Disc and Bulge cRRd stars observed by the OGLE survey (see fig. 15b of NM21; note that the OGLE photometry was through an *I*-filter and the amplitudes are min-to-max and not Fourier first-term values). In the OGLE case the bulk of the cRRd stars have $A_1(I)$ ~250 mmag, with < 1 per cent of the stars having high amplitudes and ~ 2 per cent of the stars having low amplitudes. Within the *K2* and OGLE amplitude groups A_1

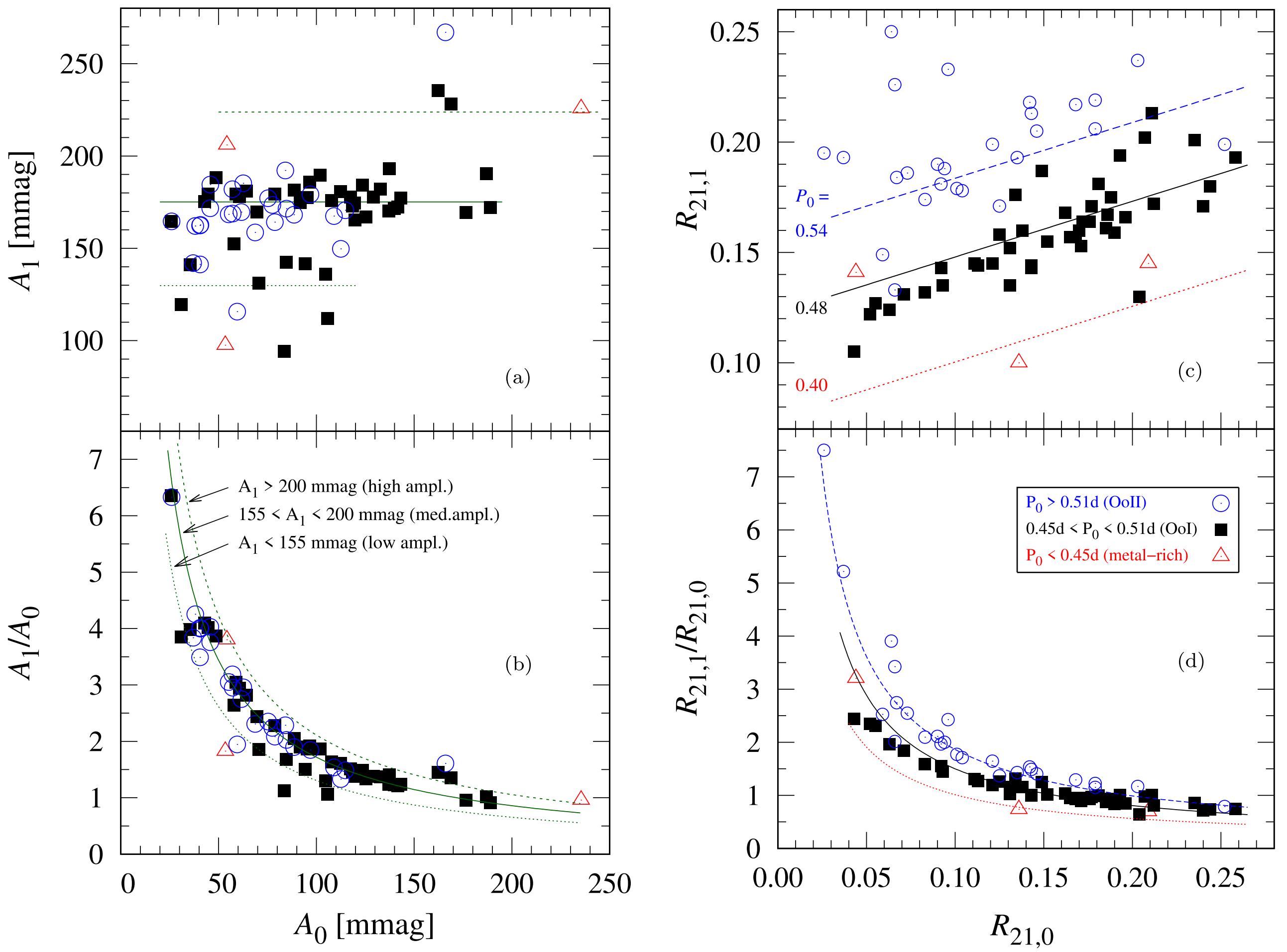

Figure 9. (a) A_1 versus A_0 diagram for the 72 cRRd stars observed by *K2* through the *Kp*-filter, where the stars have been sorted into three period groups (see the legend). (b) A_1/A_0 versus A_0 diagram for the same stars. (c) $R_{21,\,1}$ versus $R_{21,\,0}$ diagram for the same stars, with model prediction lines given for three periods: $P_0 = 0.40$ d (lower dotted line), 0.48 d (middle solid line), and 0.54 d (upper dashed line). (d) $R_{21,\,1}/R_{21,\,0}$ versus $R_{21,\,0}$ diagram, again showing a stratification by period (i.e. a family of curves).

does not appear to depend on A_0. Therefore A_1/A_0 is expected to decrease inversely with A_0, i.e. $E(A_1/A_0) = a/A_0$. In Fig. 9(b) A_1/A_0 is plotted against A_0, together with the fitted inverse relationships for the low, medium, and high amplitude groups, where the *a* values are equal to the $< A_1 >$ values given above. Agreement between the observed and predicted relationships is excellent for both *K2* and OGLE.

$R_{21,\,1}$ versus $R_{21,\,0}$ and $R_{21,\,1}/R_{21,\,0}$ versus $R_{21,\,0}$ diagrams for the *K2* cRRd stars are plotted in Figs 9(c) and (d). Unlike their amplitude counterparts (Figs 9a and b) both diagrams show a clear (but unexpected) stratification by period. For a given period $R_{21,\,1}$ increases linearly with $R_{21,\,0}$. A linear model with a common slope was fitted to the data (after checking that the slope did not vary significantly with period): $R_{21,1} = (-0.163 \pm 0.036) + (0.253 \pm 0.045)\, R_{21,0} + (0.595 \pm 0.066)\, P_0$. Three representative lines obtained by substituting $P_0 = 0.40$, 0.48, and 0.54 d are shown on the graph. The corresponding $R_{21,\,1}/R_{21,\,0}$ versus $R_{21,\,0}$ curves (i.e. above equation divided by $R_{21,\,0}$) are plotted in Fig. 9(d). Analysis of the OGLE 458 cRRd data found a similar stratification by period when $R_{21,\,1}$ was plotted against $R_{21,\,0}$, although in that case the slope increased with period. Since period depends on [Fe/H] (see the next section) this period stratification suggests that the R_{21} (light-curve shape) parameters for the two components are related to each other via metal abundance.

4.4 Metal abundances and masses

It is now well established from observations and theoretical models that RR Lyrae stars have metal abundances ranging from less than 1/100th solar (i.e. [Fe/H]<–2 dex) to greater than solar (i.e. [Fe/H]>0 dex). In this section, period-[Fe/H] calibration equations are derived and used to estimate the metal abundances of the *K2* cRRd stars. The calibration equations are based on the model given in Section 4.2 (equation 2) and are *internally consistent* with the observed Petersen diagram for cRRd stars. Metallicities and approximate masses are also given for 2130 cRRd stars observed by *Gaia*, and the effect of misclassification bias on derived [Fe/H] values is discussed.

4.4.1 Period–metallicity calibration sample

Sixteen of the 75 *K2* RRd stars were observed spectroscopically by the Sloan Digital Sky Survey (SDSS). Although the spectra are of relatively low resolution (spectrograph resolution 0.2 at 500 nm), the S/N ratios are sufficiently large to give quite accurate [Fe/H] values for 14 of the K2 stars. Effective temperatures $T_{\rm eff}$, surface gravities log g, and metallicities [Fe/H] derived by the SEGUE Stellar Parameter Pipeline (Lee et al. 2008a,b) are summarized in Table 7. Also in the table are spectrum identifiers (plate, MJD, fibre), S/N ratios and radial velocities. According to Lee (2008b), when all the systematic offsets are combined the typical uncertainty in the derived [Fe/H] values is ∼0.24 dex, which is considerably larger than the individual [Fe/H] uncertainties noted at the SDSS website. The radial velocities range from -289 ± 1 km s^{-1} to $+343 \pm 3$ km s^{-1}, consistent with the observed range for Galactic halo RR Lyrae stars. Three of the stars were observed twice, presumably at different pulsation phases.

The original plan was to use the 14 stars with SEGUE metallicities as calibrators for deriving [Fe/H] values for the entire sample of *K2* cRRd stars. However, none of the 14 stars is more metal-rich than –1.0 dex and there are only two stars with [Fe/H]<–2.0 dex. To compensate for the lack of low-metallicity calibration stars 57 cRRd stars in eight globular clusters (GCs) that have well-determined mean [Fe/H] values were added to the sample, where the metal abundances are on the 'high resolution spectra' scale of Carretta et al. (2009, hereafter C09). Since the cRRd stars within a given GC are known to show little variation in metal abundance, their metallicities are assumed to be equal to the cluster mean.[3] Pulsation periods for the two components of the GC stars were derived from B, V, I photometry from various sources.[4] The periods were checked using the same methods that were used to analyse the *K2* RRd stars. Agreement across filters and with previously published values was excellent.

Also added to the calibration sample were 207 cRRd stars with SDSS/SEGUE metallicities and Zwicky Transient Facility (ZTF, DR14) photometry (Chen et al. 2023).[5] Ten of the 14 *K2* calibration stars were found to be in common with the Chen sample. The remaining 197 Chen et al. stars have an overall distribution that closely matches that of the *K2* stars but includes many more low-metallicity stars. The Chen sample, like the *K2* sample, does not include short-period (i.e. $P_0 < 0.45$ d) cRRd stars. Chen et al. do not provide amplitudes or Fourier parameters.

4.4.2 *Period–[Fe/H] calibration*

Panels (a) and (b) of Fig. 10 show, for the combined *K2*+GC+Chen metallicity calibration sample ($N = 268$), the relationships between P_0, P_1, P_1/P_0, and [Fe/H]. The fitted curves in the four panels are based on the model given by equation (2), where $X =$ [Fe/H] is assumed to be a common factor linking the periods. In Fig. 10(a) the fitted lines relating $\sqrt{P_0}$ and $\sqrt{P_1}$ to [Fe/H] are plotted. The estimated slopes, $b_0 = -0.0564 \pm 0.0020$ and $b_1 = -0.0497 \pm 0.0018$, differ significantly ($p < 0.0001$), i.e. the lines are not parallel. Notice that equation (2) implies (by squaring both sides and calculating the mean) that the mean period for a given [Fe/H] is non-linear in [Fe/H] for both pulsation modes:

$$E(P_0) = \left(a_0 + b_0[\mathrm{Fe/H}]\right)^2 + \sigma_0^2$$
$$E(P_1) = \left(a_1 + b_1[\mathrm{Fe/H}]\right)^2 + \sigma_1^2. \qquad (6)$$

Since $b_0 \neq b_1$ the difference between the mean periods depends on [Fe/H], which contradicts the Braga et al. (2022) conclusion that 'their difference is constant over a broad range in pulsation periods and in metal abundance.'

In Fig. 10(b) the ratio P_1/P_0 is plotted against [Fe/H]. The ratio of the mean periods (equation 6), which, using a first-order Taylor expansion, is approximately equal to the mean of P_1/P_0, is also plotted. A similar diagram was plotted by Braga et al. (2022), who fitted a line to their data (see their equation 2 and fig. 9). Owing to the relatively large scatter and limited [Fe/H] range of both samples (−1.0 to −2.5 dex) it is difficult to determine from the data which form provides a better fit. However, a linear relationship between P_1/P_0 and [Fe/H] can be ruled out because it is inconsistent with the assumed quadratic relationships between the individual periods and [Fe/H] (Fig. 10a). Notice also that there would be a similar lack of consistency if the P_0–[Fe/H] and P_1–[Fe/H] relationships were assumed to be linear.

To validate the functional form of the equation (2) model, equation (4) was fitted to the combined sample of *K2* + OGLE cRRd stars shown in Fig. 1. This sample includes the 72 *K2* cRRd stars and the 458 OGLE Galactic Disc and Bulge cRRd stars from Soszyński et al. (2019), and spans the entire period range of known cRRd stars, $0.35 < P_0 < 0.62$ d. The fitted curve is given by equation (4) with $a = -0.1634 \pm 0.0032$, $b = 0.4359 \pm 0.0093$, and $c = 0.4552 \pm 0.0068$, where the rms-error is 0.0007, and is plotted with a solid black line in Figs 1 and 10(c). Equation (4) was also fitted to the cRRd stars shown in the Petersen diagram plotted in Fig. 10(c). In this case the sample of cRRd stars consists of the 268 metallicity calibration stars (*K2*+GC+Chen) plus the 58 *K2* stars not included in the metallicity calibration (i.e. those stars with unknown spectroscopic [Fe/H]). The fit is plotted as a black dashed curve in Fig. 10(c), where the coefficients are $a = -0.1870 \pm 0.0115$, $b = 0.5023 \pm 0.0323$, $c = 0.4088 \pm 0.0227$, with rms-error 0.0005. The red dotted curve in Fig. 10(c) was obtained by fitting equation (5) to the same data, where now the coefficients are $a' = -0.0085 \pm 0.0003$ and $b' = 0.7617 \pm 0.0006$, with rms-error 0.0007. Comparison of the three fitted curves shows that the equation (4) curves (black) are consistent with the two samples, while the equation (5) curve (red dotted) is not (see Section 4.2).

Figs 10(a)–(c) demonstrate that the equation (2) model provides a solid framework relating P_0, P_1, and [Fe/H]. The model fits the observations and is internally consistent. Inverting and fitting equation (2) gives the following period–metallicity calibration curves:

$$[\mathrm{Fe/H}] = (7.59 \pm 0.34) - (13.25 \pm 0.47)\sqrt{P_0}$$
$$[\mathrm{Fe/H}] = (7.42 \pm 0.33) - (15.08 \pm 0.53)\sqrt{P_1}, \qquad (7)$$

where in both cases the root-mean-square error is ±0.17 dex, and the standard errors of the mean typically are ± 0.01 dex (rising to ± 0.04 dex at the extremes of the period ranges). Either equation can be used to estimate metal abundance. The calibration curve plotted in Fig. 10(d) is the P_0 version, which is used below for deriving metallicities for cRRd stars with P_0 in the range 0.45–0.59 d.

[3]This would not be the case in most dwarf galaxies, in particular the higher luminosity systems (see Braga et al. 2022) where the stars are observed to have a range of metallicities.

[4]Sources of the photometry (and preliminary periods) for the GC RRd stars: M68 (Clement et al. 1993; Brocato, Castellani & Ripepi 1994; Walker 1994; Kains et al. 2015a,b), M15 (Sandage et al. 1981; Bingham et al. 1984; Nemec 1985b; Corwin et al. 2008), NGC 2257 (Nemec, Walker & Jeon 2009), IC 4499 (Clement et al. 1986; Walker & Nemec 1996; Kunder et al. 2011); M3 (Nemec & Clement 1989); Reticulum (Kuehn et al. 2013); NGC 2419 (Clement & Nemec 1990; Di Criscienzo et al. 2011) and NGC 6426 (Clement & Nemec 1990; Hatzidimitriou et al. 1999).

[5]An additional 96 cRRd stars with LAMOST metallicities (and ZTF photometry) were identified by Chen et al., five of which are in common with the *K2* sample. However, owing to apparent systematic differences between the LAMOST and SEGUE metallicities only the Sloan [Fe/H] values for the Chen stars have been considered in this paper.

Table 7. Physical characteristics for the 16 *K2* RRd stars with SDSS spectra, from which [Fe/H] values were derived for 14 stars by the SEGUE Stellar Parameter Pipeline (Lee et al. 2008a,b). All are classical RRd stars. The individual spectra are identified by the plate number, the Modified Julian Date (MJD-2400000), and the optical fibre number (columns 2–4), and the signal-to-noise ratios (column 5) are per pixel *r*-band median values. The subheaders for $T_{\rm eff}$, log *g*, and [Fe/H] (columns 7–12) are the stellar parameter names from the SEGUE 'sppParams' table.

EPIC	SDSS spectrum			S/N	RV	$T_{\rm eff}$(K)		log *g*		[Fe/H]	
	plate	MJD	fiber		[km/s]	TEFFADOP	TEFFSPEC	LOGGADOP	LOGGSPEC	FEHADOP	FEHSPEC
(1)	(2)	(3)	(4)	(5)	(6)	(7)	(8)	(9)	(10)	(11)	(12)
60018662 (E2)	1903	53357	469	100.2	−289 ± 1	6945 ± 95	7074 ± 75	3.65 ± 0.27	3.54 ± 0.30	−2.06 ± 0.08	−2.18 ± 0.08
201585823 (C1)	514	51994	47	43.0	−62 ± 2	7156 ± 95	7078 ± 59	3.88 ± 0.03	3.91 ± 0.02	−1.57 ± 0.03	−1.57 ± 0.03
211694449 (C5,18)	2274	53726	435	31.2	+ 67 ± 3	7108 ± 75	6990 ± 80	3.12 ± 0.42	3.09 ± 0.34	−1.23 ± 0.02	−1.26 ± 0.03
	3230	54860	195	46.8	+ 62 ± 2	6955 ± 73	6842 ± 86	2.84 ± 0.28	2.66 ± 0.28	−1.42 ± 0.09	−1.37 ± 0.09
211888680 (C5,16)	2283	53729	32	11.2	+ 53 ± 10	7046 ± 94	7174 ± 55	2.80 ± 0.40	2.74 ± 0.65	−1.73 ± 0.05	−1.68 ± 0.04
211898723 (C5,18)	2273	53709	416	34.0	+ 343 ± 3	6834 ± 91	6957 ± 93	3.68 ± 0.27	3.74 ± 0.31	−1.72 ± 0.01	−1.55 ± 0.11
220254937 (C8)	7860	57006	232	33.3	−135 ± 3	...	...	...	...	...	...
201440678 (C10)	286	51999	181	29.9	+ 216 ± 4	7232 ± 107	7413 ± 88	3.17 ± 0.33	3.02 ± 0.08	−2.02 ± 0.18	−1.93 ± 0.02
	2892	54552	144	32.2	+ 240 ± 4	6766 ± 63	6731 ± 79	2.42 ± 0.28	2.58 ± 0.29	−1.92 ± 0.04	−1.92 ± 0.04
201519136 (C10)	288	52000	577	33.8	−63 ± 3	6838 ± 46	6861 ± 71	2.96 ± 0.16	3.07 ± 0.11	−1.40 ± 0.04	−1.37 ± 0.06
228800773 (C10)	2707	54144	442	35.0	+ 188 ± 3	6781 ± 52	6814 ± 75	2.98 ± 0.13	2.93 ± 0.14	−1.91 ± 0.08	−1.82 ± 0.06
248369176 (C10)	2568	54153	234	7.9	−17 ± 18	...	...	...	...	...	...
	3847	55588	480	3.7	−40 ± 15	...	...	...	...	...	...
201749391 (C14)	3242	54889	569	56.6	−170 ± 2	6721 ± 43	6691 ± 61	3.35 ± 0.15	3.40 ± 0.17	−1.46 ± 0.01	−1.46 ± 0.01
248426222 (C14)	275	51910	382	33.8	+ 203 ± 3	6939 ± 51	6987 ± 25	3.26 ± 0.28	3.42 ± 0.27	−2.20 ± 0.02	−1.94 ± 0.18
248845745 (C14)	1600	53090	636	20.4	−11 ± 5	7099 ± 11	7326 ± 158	3.23 ± 0.33	3.21 ± 0.43	−1.60 ± 0.17	−1.60 ± 0.01
248871792 (C14)	1602	53117	326	50.2	+ 215 ± 1	7277 ± 92	7416 ± 87	3.43 ± 0.16	3.37 ± 0.18	−1.69 ± 0.07	−1.68 ± 0.02
211665293 (C16)	2435	53828	249	43.0	−33 ± 3	6979 ± 83	6904 ± 8	4.18 ± 0.63	4.26 ± 0.08	−1.58 ± 0.04	−1.58 ± 0.04
251629085 (C17)	3307	54970	230	64.1	+ 31 ± 1	6989 ± 75	6906 ± 65	3.10 ± 0.23	3.08 ± 0.30	−1.47 ± 0.06	−1.40 ± 0.07

4.4.3 *Metallicities and masses for the K2 cRRd stars*

Metal abundances for the 72 *K2* cRRd stars obtained by applying equation (7) are given in Table 8, where the stars are ordered by increasing P_0. Also in the table are *Gaia* Identification numbers for the 53 stars in common with ESA's *Gaia* Mission (col. 3; see Section 4.4.4), the *Gaia* DR2 and DR3 RR Lyrae classifications (cols. 4 and 5), fundamental-mode periods and period ratios (cols. 6 and 7). Approximate masses for the *K2* cRRd stars were estimated by substituting P_1/P_0 and Z into the following formula derived specifically for RRd stars by Marconi et al. (2015, equation 5) from hydrodynamical models:

$$\log M/M_{\odot} = -0.85(\pm 0.05) - 2.8(\pm 0.3)\log(P_1/P_0) - 0.097(\pm 0.003)\log Z, \qquad (8)$$

where Z represents the fraction by mass of elements heavier than hydrogen and helium, and is related to [Fe/H] according to [Fe/H] $= \log Z/Z_{\odot}$ (assuming $X = X_{\odot}$). In this paper the values adopted for the Sun are $Z_{\odot} = 0.0139 \pm 0.0006$ and $X_{\odot} = 0.7438 \pm 0.0054$ (Asplund, Amarsi & Grevesse 2021). Column 9 of Table 8 contains the mass based on scaled solar abundances and assuming no enhancement with respect to iron of the α-elements (O, Ne, Mg, Si, S, and C), i.e. [α/Fe] $= 0$, in which case $\log Z =$ [Fe/H] $-$ 1.857. Column 10 contains the mass derived assuming an α-element enhancement [α/Fe] $= +0.30$ dex (i.e. the average α-element abundance is twice the scaled solar value), in which case $\log Z =$ [Fe/H] $-$ 1.635, where the constant follows from the VandenBerg et al. (2000, tables 1 and 2; 2006, table 1) metallicities after adjusting to correct for $Z_{\odot} = 0.0188$ assumed by VandenBerg. The resulting mass estimates range from $\sim$0.57 $M_{\odot}$ for the most metal-rich stars in the sample to 0.81 $M_{\odot}$ for the most metal-poor stars, with the α-enhanced masses typically $\sim$0.03 $M_{\odot}$ smaller than the [α/Fe] $= 0$ case. The derived mass range for the RRd stars is consistent with the range established from horizontal-branch evolution models (see VandenBerg & Denissenkov 2018), from hydrodynamical models (Molnár et al. 2015) and from asteroseismology (Netzel et al. 2023).

4.4.4 Gaia *observations of the* K2 *RRd stars*

The 75 RRd stars observed by *K2* were matched using RA and DEC coordinates to the *Gaia* DR2 and DR3 RR Lyrae catalogues (Clementini et al. 2019, 2023). Fifty-four stars were found in one or both of the catalogues: the 53 cRRd stars identified in col. 2 of Table 8, and one of the three aRRd stars (EPIC 205209951). The RR Lyrae types given by *Gaia* were 'obtained using the period–amplitude diagram in the *G*-band, the plots of the Fourier parameters R_{21} and ϕ_{21} versus period, and the Petersen diagram' (see fig. 7 of Clementini et al. 2023). Of the 49 *K2* cRRd stars listed in DR3 (see col.5 of Table 8) only five were correctly classified 'RRd' (10 per cent), 41 were misclassified 'RRc' (84 per cent) and three were misclassified 'RRab' (6 per cent). Five of the 24 *K2* cRRd stars in DR2 (see col. 4 of Table 8) were correctly classified 'RRd' (21 per cent), 17 were misclassified 'RRc' (71 per cent) and two were misclassified 'RRab' (8 per cent). Only one of the 20 stars found in both *Gaia* catalogues was correctly classified in both (see also Molnar et al. 2018) .

Comparison of the periods given in the DR3 catalogue with those in Table 3 reveals that only the first-overtone period was detected in all the cRRd stars misclassified 'RRc' (and in three of the five stars misclassified 'RRab'), i.e. only the shorter-period higher-amplitude component was detected. This suggests that a significant number of 'RRc' stars (and possibly some 'RRab' stars) in the *Gaia* catalogues may actually be cRRd stars. Moreover, for two of the nine *K2* stars correctly classified 'RRd' in DR2 or DR3, the *Gaia* fundamental period and period-ratio differ from the high-precision *K2* values given in Table 3 by amounts that place the stars significantly above or below the Petersen curve for cRRd stars.

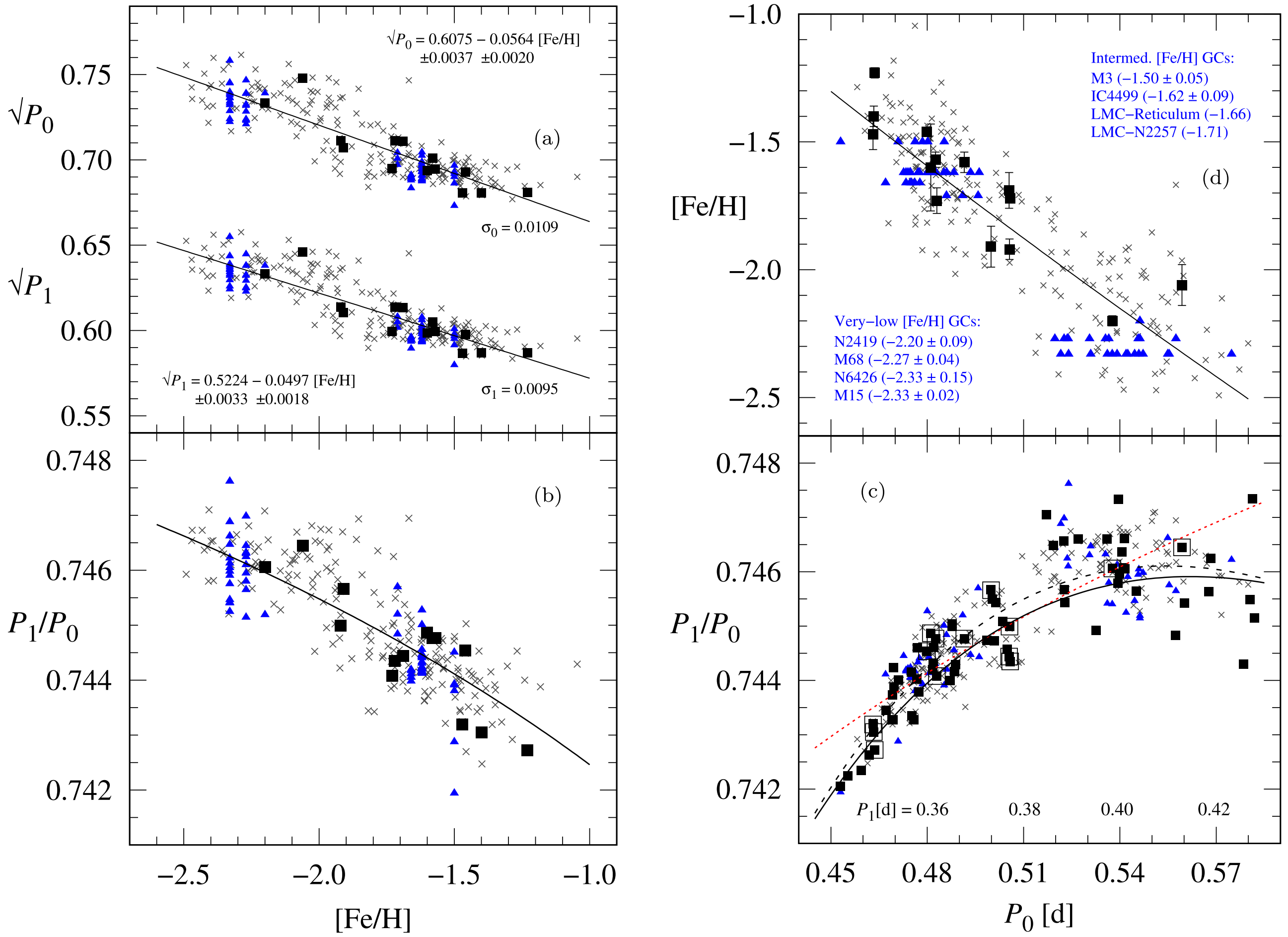

Figure 10. Period–metallicity relations and Petersen diagram for 'classical' RRd (cRRd) stars. The symbols are as follows: filled squares for the 14 *K2* cRRd calibration stars with SDSS/SEGUE metallicities, filled triangles for the 57 cRRd stars in eight globular clusters that have well-established mean [Fe/H] values, and crosses for the 197 non-*K2* Chen et al. (2023) calibration stars with SDSS/SEGUE metallicities. The fitted regression curves are discussed in the text. (a) Period–metallicity relations for the fundamental and first-overtone pulsation periods of the calibration cRRd stars. (b) Period-ratio versus metallicity diagram for the calibration stars. (c) Petersen diagram for the cRRd metallicity calibration stars and 58 *K2* stars not included in the calibration sample (the *K2* calibration stars are identified with boxes around the solid squares). The three Galactic Bulge *K2* stars with $P_0 < 0.45$ d and period ratios <0.742 are off-scale (but can be seen in Fig. 1). (d) Metallicity versus period graph for cRRd stars, where the abscissa is the fundamental period, P_0. The assumed mean metallicities of the GCs are noted on the graph.

4.4.5 Metallicities and masses for 2130 Gaia *cRRd stars*

The latest *Gaia* Survey, DR3 (Clementini et al. 2023), gives photometric [Fe/H] estimates for 113202 (65 per cent) of the 175350 stars classified 'RRab' and for 20375 (22 per cent) of the 94422 stars classified 'RRc'. No metal abundances are reported for the 2378 stars classified 'RRd' in DR2 or for the 2007 stars classified 'RRd' in DR3. To fill in this gap equation (6) was applied to those stars classified 'RRd' in one or both *Gaia* catalogues, and which have periods and period ratios within the ranges of the [Fe/H] calibration data, i.e. $0.45 < P_0 < 0.59$ d and $0.7418 < P_1/P_0 < 0.7477$ (see Fig. 10), and which lie on or close to the Petersen curve. A total of 2253 of the 3714 stars classified 'RRd' in either DR2 or DR3 have periods and period ratios within the [Fe/H] calibration range. Of the 2253 stars, 123 have locations more than 2σ above or below the '*K2* + OGLE' Petersen curve shown in Fig. 1 (i.e. with $|\Delta(P_1/P_0)| > 0.0014$) and were eliminated, leaving 2130 stars. A Petersen diagram for the 2130 'presumably *bona fide*' cRRd stars is shown in Fig. 11, together with the 'K2+OGLE' Petersen curve (Fig. 1). The distribution of the 623 stars classified 'RRd' in both catalogues (plotted with black filled dots) is similar to that of the 1507 stars classified 'RRd' only in one or the other but not both (blue crosses).

Metallicities and masses for the 2130 *Gaia* cRRd stars are given in Table 9. Also in the table are *Gaia* identification numbers (usually from DR3),[6] coordinates of the stars (RA,DEC), the RR Lyr

[6] *Gaia* identification numbers are usually the same in DR2 and DR3, but not always. An example of where this is not the case is RR Lyrae itself: in DR2 it is 2125982599341232896, and in DR3 it is 2125982599343482624, the difference occurring in the last seven digits. Of the stars classified 'RRd' in either DR2 or DR3, 93 stars were found to have similar coordinates (RA,DEC) but different identification numbers (again, the differences tending to occur in the last ~8 digits of the 19 digit number). A match by RA and DEC revealed that 93 of the 3714 stars classified 'RRd' in either DR2 or DR3 were found to have different *Gaia* identification numbers in DR2 and DR3. The 93 stars are identified in Table 10. Also given in the table are the periods and period-ratios given in DR2 and DR3; close agreement of the DR2 and DR3 periods and period-ratios increases the confidence that it is the same star. The last column indicates whether or not the star is a 'classical' RRd star within 2σ of the K2+OGLE Petersen curve.

Table 8. Metal abundances and masses for the 72 cRRd stars observed during NASA's *K2* Mission. The values for the three shortest period stars are enclosed in parentheses because they are outside the period range of the [Fe/H] calibration curve. *Gaia* IDs and classifications are also given for the 53 cRRd stars in common with either DR2 or DR3. The masses were derived assuming no enhancement of α elements with respect to iron (i.e. [α/Fe] = 0.0 dex), and an enhancement [α/Fe] = 0.3 dex.

EPIC No. (1)	K2 Campaign (2)	*Gaia* Identification no. (3)	*Gaia* classif. DR2 (4)	DR3 (5)	P_0 (d) (6)	P_1/P_0 (7)	[Fe/H] ± 0.17 dex (8)	M/M$_\odot$ [α/Fe] = 0.0 (9)	[α/Fe] = 0.3 (10)
225456697	C11	...	...	...	0.399838	0.73618	(–0.79)	(0.57)	(0.57)
251248830	C11	...	...	...	0.419592	0.73885	(–1.00)	(0.62)	(0.59)
251248826	C11	4059683185121550336	...	RRc	0.430234	0.73982	(–1.11)	(0.64)	(0.61)
246058914	C12	2438582821787698176	RRab	...	0.452948	0.74205	−1.33	0.66	0.63
251248827	C11	...	...	...	0.455268	0.74224	−1.35	0.67	0.63
229228184	C7	4071397068375975296	RRc	RRc	0.459430	0.74234	−1.40	0.67	0.64
224366356	C9	...	...	...	0.461936	0.74263	−1.42	0.68	0.64
251629085	C17	3686704514188694144	RRc	RRc	0.463110	0.74320	−1.43	0.68	0.64
201519136	C10	3699831549153899648	RRd	RRd	0.463376	0.74305	−1.43	0.68	0.64
211694449	C5,18	...	...	...	0.463650	0.74272	−1.44	0.68	0.65
251809814	C17	...	...	...	0.467124	0.74345	−1.47	0.68	0.65
251456808	C12	...	...	...	0.468980	0.74328	−1.49	0.68	0.65
236212613	C11	4107786711365354496	RRc	RRd	0.469200	0.74373	−1.49	0.68	0.65
212615778	C17	3624326573845415552	RRab	RRc	0.469391	0.74328	−1.49	0.68	0.65
212455160	C6,17	...	...	...	0.469592	0.74388	−1.49	0.68	0.65
229228175	C7	4071509081124919040	RRc	RRc	0.469540	0.74424	−1.49	0.68	0.65
248653210	C14	3862737081709822208	...	RRc	0.471007	0.74401	−1.51	0.69	0.65
245974758	C12	...	...	...	0.475291	0.74335	−1.55	0.69	0.66
212819285	C17	...	...	...	0.474968	0.74415	−1.55	0.69	0.66
251809825	C17	3630514930231792128	...	RRd	0.475900	0.74328	−1.56	0.69	0.66
220604574	C8	2579544339932337152	...	RRc	0.476772	0.74403	−1.56	0.69	0.66
212335848	C6	3604456989982044800	...	RRc	0.476856	0.74460	−1.56	0.69	0.66
251809772	C17	...	...	...	0.477332	0.74379	−1.57	0.70	0.66
201749391	C14	...	...	...	0.479930	0.74454	−1.59	0.70	0.66
248845745	C14	3870825497264938752	...	RRc	0.481123	0.74487	−1.61	0.70	0.66
201152424	C10	3596646712214016768	...	RRc	0.481725	0.74420	−1.61	0.70	0.67
210933539	C4	61543999430570496	RRd	...	0.481801	0.74432	−1.61	0.70	0.67
248667792	C14	3863597548342360448	...	RRc	0.482054	0.74461	−1.61	0.70	0.67
211888680	C5,16	612194609624700928	RRc	RRc	0.482993	0.74408	−1.62	0.70	0.67
201585823	C1	3796490612783265152	RRc	RRc	0.482590	0.74477	−1.62	0.70	0.67
210600482	C4	44250085978293504	...	RRc	0.487191	0.74400	−1.66	0.71	0.68
229228220	C7	4073132888018172160	...	RRc	0.487740	0.74504	−1.67	0.71	0.67
212449019	C6	3620942277055055488	RRc	RRc	0.487778	0.74499	−1.67	0.71	0.67
251809860	C17	...	...	...	0.488442	0.74416	−1.67	0.71	0.68
210831816	C4	51156844364167552	RRd	RRc	0.488793	0.74429	−1.68	0.71	0.68
211665293	C16	610414019262262912	RRc	RRd	0.491516	0.74477	−1.70	0.71	0.68
212498188	C17	...	...	...	0.498643	0.74474	−1.77	0.72	0.69
228800773	C10	...	...	...	0.499880	0.74567	−1.78	0.72	0.69
229228811	C8	2576293393286532224	RRc	RRc	0.500219	0.74550	−1.79	0.73	0.69
251521080	C17	3684381207464081792	...	RRab	0.500870	0.74473	−1.79	0.73	0.69
220636134	C8	2580012972403894528	RRc	RRc	0.501375	0.74543	−1.80	0.73	0.69
213514736	C7	...	...	...	0.503583	0.74509	−1.82	0.73	0.70
251809870	C17	...	...	...	0.504830	0.74457	−1.83	0.73	0.70
248871792	C14	3872607878628627840	RRc	RRab	0.505497	0.74444	−1.83	0.74	0.70
201440678	C10	3698706061563300608	RRd	RRc	0.505614	0.74499	−1.84	0.73	0.70
211898723	C5,18	662527846763392000	...	RRc	0.505827	0.74435	−1.84	0.74	0.70
212467099	C17	3609194923025131648	...	RRc	0.517170	0.74705	−1.94	0.75	0.71
251809832	C17	3606923499505619968	...	RRc	0.519190	0.74648	−1.96	0.75	0.72
248730795	C14	3869100230377688448	...	RRc	0.522545	0.74657	−1.99	0.76	0.72
229228194	C7	4071405658308934144	RRc	...	0.522630	0.74567	−1.99	0.76	0.72
248827979	C14	...	...	...	0.522807	0.74543	−1.99	0.76	0.72
211072039	C4	54010936031517440	...	RRc	0.527041	0.74660	−2.03	0.76	0.73
250056977	C15	6265195826928713600	...	RRc	0.532603	0.74492	−2.08	0.78	0.74
220254937	C8	2558508311670941824	...	RRc	0.535934	0.74660	−2.11	0.78	0.74
248426222	C14	3807285480505638784	...	RRc	0.537644	0.74606	−2.13	0.78	0.74
060018653	E2	2739784862463040512	RRd	RRc	0.539441	0.74579	−2.15	0.79	0.75
247334376	C13	3414155402936376832	...	RRc	0.539580	0.74733	−2.15	0.78	0.74
248653582	C14	3865590520542557184	...	RRab	0.539878	0.74596	−2.15	0.79	0.75
228952519	C10	3682596906250805632	RRc	RRc	0.540600	0.74637	−2.16	0.79	0.75
214147122	C7	4072051140361909632	RRc	RRc	0.541040	0.74607	−2.16	0.79	0.75

Table 8 – *continued*

EPIC No. (1)	K2 Campaign (2)	*Gaia* Identification no. (3)	*Gaia* classif. DR2 (4)	DR3 (5)	P_0 (d) (6)	P_1/P_0 (7)	[Fe/H] ± 0.17 dex (8)	M/M$_\odot$ [α/Fe] = 0.0 (9)	[α/Fe] = 0.3 (10)
251248825	C11	4059675454173637632	...	RRc	0.541343	0.74661	−2.16	0.79	0.75
235794591	C11	4059476025896752384	RRc	...	0.541583	0.74605	−2.17	0.79	0.75
212547473	C6,17	3610631916003219328	RRc	RRc	0.545079	0.74564	−2.20	0.79	0.76
248509474	C14	3856963644936004352	...	RRc	0.557312	0.74483	−2.31	0.82	0.78
060018662	E2	2642992895363833088	...	RRc	0.559323	0.74645	−2.32	0.81	0.78
248731983	C14	3869066244300744064	...	RRc	0.560084	0.74542	−2.33	0.82	0.78
223051735	C9	...	...	...	0.567737	0.74563	−2.40	0.83	0.79
248369176	C10	3698207256945765760	RRc	RRd	0.568280	0.74625	−2.40	0.83	0.79
249790928	C15	6255192229621483136	...	RRc	0.578550	0.74430	−2.49	0.85	0.81
235631055	C11	4059259044129556352	...	RRc	0.580463	0.74549	−2.51	0.85	0.81
248514834	C14	3857004812197962880	...	RRc	0.581287	0.74734	−2.52	0.85	0.81
225326517	C11	4116711825239025152	...	RRc	0.581816	0.74515	−2.52	0.86	0.81

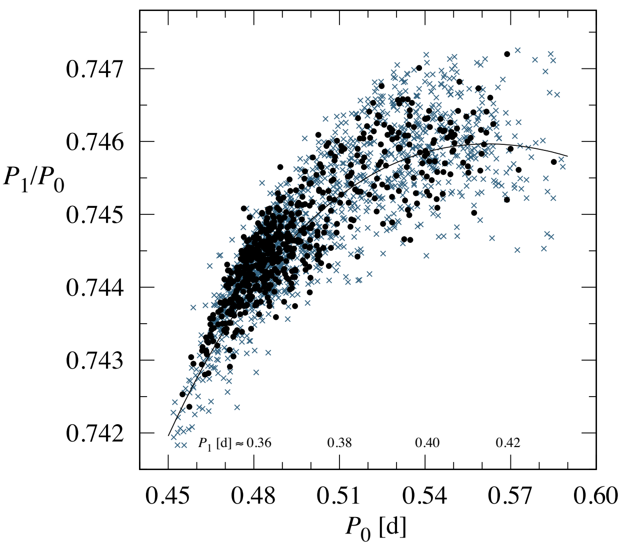

Figure 11. Petersen diagram for 2130 *Gaia* cRRd stars. The 1507 crosses represent the stars classified 'RRd' in either DR2 or DR3 but not both, and the 623 dots represent the stars classified 'RRd' in both catalogues (see Table 9). Also shown is the long-period portion of the '*K2* + OGLE' Petersen curve (solid curves in Figs 1 and 10c).

classifications given in DR2 and DR3, pulsation periods and period ratios, and masses. If the star is listed in DR3 then the periods from that catalogue were used to calculate [Fe/H], otherwise the periods from DR2 were used. The resulting [Fe/H] values range from –1.32 to –2.58 dex, with uncertainties of ± 0.17 dex, and the masses range from 0.63 to 0.86 $M_\odot$. Until more is known about their physical characteristics equation (7) should not be applied to aRRd or pRRd stars or any other stars that deviate significantly from the Petersen curve. The masses were calculated using the same Marconi et al. formula used to derive masses for the K2 cRRd stars, again both without and with α-element abundance enhancements.

4.4.6 *Misclassification bias*

In Fig. 12 the period–metallicity relations for single-mode RRab and RRc stars are compared with the [Fe/H] calibration curves for cRRd stars (equation 6). The figure also illustrates the effect on the derived metal abundance of misclassifying a cRRd star as 'RRab' or 'RRc'. The period-[Fe/H] diagram plotted in Fig. 12(a) (left panel) includes 208 RR Lyr stars having spectroscopic metal abundances derived from high-resolution spectra by Crestani et al. (2021b; tables 2 and 6). The thicker portions of the cRRd calibration curves (equation 7) correspond to the period ranges of the calibration stars (see Fig. 10) and the dashed portions represent extrapolations beyond these ranges.

Table 9. Metallicities and masses for the 2130 *Gaia* stars classified 'RRd' by either DR2 or DR3 and that are on the cRRd curve in the Petersen diagram (see Fig. 11). The [Fe/H] values (col. 9) were estimated using the P_0-[Fe/H] calibration formula (equation 7). The masses estimates were made assuming no α-element enhancements (col.10) and assuming α element abundances enhanced by a factor two (col.11). The complete table is given online in the Supporting Information.

Gaia Id (1)	RA (2016.0) (2)	DEC (3)	*Gaia* Classif. DR2 (4)	DR3 (5)	P_1 (d) (6)	P_0 (d) (7)	P_1/P_0 (8)	[Fe/H] ± 0.17 (9)	M/M$_\odot$ [α/Fe] = 0.0 (10)	[α/Fe] = 0.3 (11)
4109411961354217856	258.5835748	−25.70825502	RRab	RRd	0.335361	0.451800	0.74228	−1.32	0.66	0.63
1797412030619582848	323.6745277	+23.89800184	RRd	RRc	0.335297	0.451917	0.74194	−1.32	0.66	0.63
6028840233297277440	258.3737969	−29.79608735	RRd	RRc	0.335828	0.452341	0.74242	−1.33	0.66	0.63
1494770600375550336	218.7012557	+46.44626505	...	RRd	0.336212	0.453218	0.74183	−1.33	0.66	0.63
6786048671278168448	322.7495052	−29.83430933	...	RRd	0.336362	0.453317	0.74200	−1.34	0.66	0.63
4541576557133679360	259.6822537	+13.59407288	...	RRd	0.336546	0.453436	0.74221	−1.34	0.66	0.63
6582029310878687104	320.4805041	−41.500339	...	RRd	0.337054	0.454214	0.74206	−1.34	0.67	0.63
4686535719166593408	22.66688193	−72.73111643	RRd	RRd	0.337847	0.454993	0.74253	−1.35	0.67	0.63
3464599248369119104	176.9940688	−35.49997468	RRd	RRc	0.337824	0.455095	0.74231	−1.35	0.67	0.63
5341057708232415104	165.5449429	−55.53852362	RRab	RRd	0.337885	0.455360	0.74202	−1.36	0.67	0.64
...										

Table 10. Ninety-three *Gaia* stars classified 'RRd' in DR2 or DR3, with similar RA,DEC coordinates but different identification numbers in DR2 and DR3. The complete table is given online in the Supporting Information.

	Gaia DR2					*Gaia* DR3				
DR2 Identification No.	RR class	P_1 (d)	P_0 (d)	P_1/P_0	DR3 Identification No.	RR class	P_1 (d)	P_0 (d)	P_1/P_0	cRRd?
(1)	(2)	(3)	(4)	(5)	(6)	(7)	(8)	(9)	(10)	(11)
1442424496748916480	RRd	0.404211	0.541729	0.74615	1442424501044402432	RRd	0.404205	0.541687	0.74620	yes
1470192632844893568	RRd	0.382444	0.513261	0.74513	1470192632845260288	RRd	0.382446	0.513238	0.74516	yes
1554867810007895296	RRd	0.350923	0.471790	0.74381	1554867810004952192	RRd	0.350912	0.471762	0.74383	yes
1639360120343239808	RRc	0.361888	...	...	1639360124638557440	RRd	0.361899	0.486449	0.74396	yes
1745948362385628416	RRab	...	0.567080	...	1745948362391096832	RRd	0.413354	0.554544	0.74539	yes
2510409037347211264	RRab	...	0.353731	...	2510409041642733568	RRd	0.353735	0.475571	0.74381	yes
2862259978075970816	RRd	0.397965	0.534996	0.74387	2862259978077052160	RRab	...	0.534997	...	no
2972392044878569984	RRd	0.385688	0.516862	0.74621	2972392044879268096	RRc	0.385673	...	...	yes
3059619325966429824	RRd	0.396827	0.542776	0.73111	3059619325975593600	RRab	...	0.542772	...	no
3746580820769812096	RRc	0.394827	...	...	3746580825061729536	RRd	0.394837	0.528923	0.74649	yes
...										

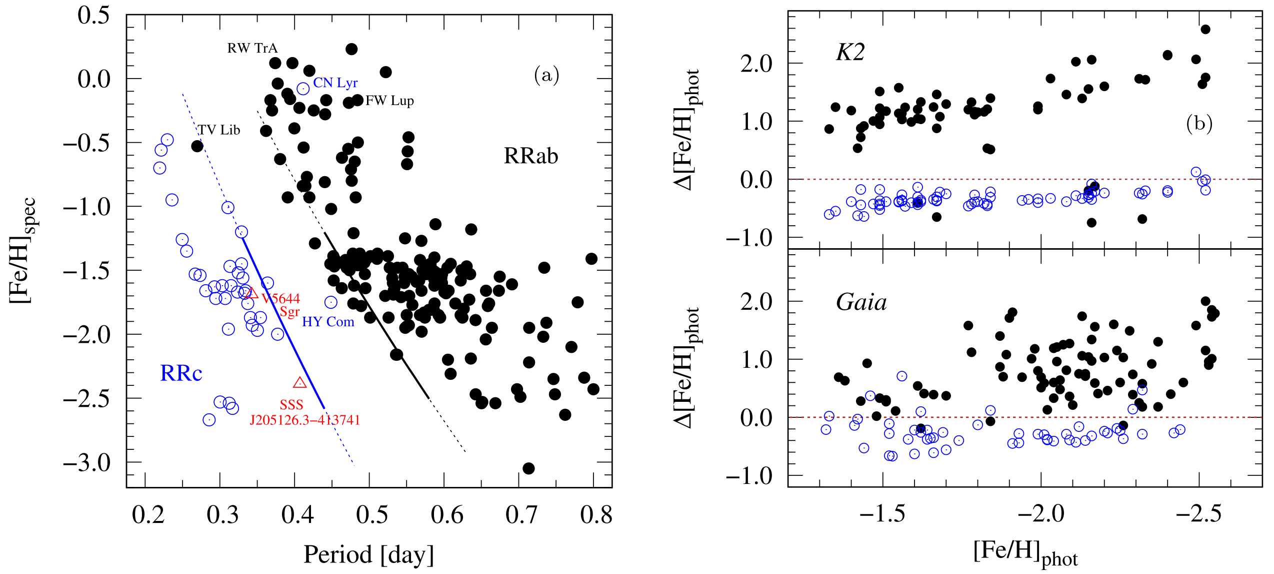

Figure 12. (a) Period–metallicity diagram for 206 single-mode RRab or RRc stars (and two possible RRd stars) with $[Fe/H]_{spec}$ values derived from high-resolution spectra (Crestani et al. 2021a,b). The diagonal 'lines' are the first-overtone and fundamental mode metallicity regressions for cRRd stars, and the labelled stars are discussed in the text. (b) Misclassification error, $\Delta[Fe/H]_{phot}$, as a function of metal abundance for the 72 *K2* cRRd stars (top panel), and for 131 cRRd stars misclassified in the *Gaia* DR2 or DR3 catalogues (bottom panel), where the solid dots correspond to the bias if misclassified 'RRab', the open circles to the bias if misclassified 'RRc'.

The graph shows that the cRRd relationship for the first-overtone (left) coincides with the long-period edge for the RRc stars, and the fundamental-mode curve (right) coincides with the short-period edge for the RRab stars, with a clear gap separating the two types of stars. As previously observed, both RR Lyr types show a tendency to increase in metallicity with decreasing pulsation period (see figs 12 and 13 of Nemec et al. 2013; and fig. 7 of Sneden et al. 2018).

Seven stars labelled in Fig. 12(a) have unusual locations or questionable RR Lyr types. The pulsation period for TV Lib (0.270 d) is extremely short for an 'RRab star (Kovacs 2005), and the period for HY Com (0.449 d) is long for an 'RRc' star. V5644 Sgr and SSS J205126.3-413741 may be RRd stars but the evidence is inconclusive: V5644 Sgr is classified 'RRd' by Crestani et al. but 'RRab' by *Gaia* DR3; and SSS J205126.3-413741 is classified 'RRc' by Crestani et al. but 'RRd' in DR2 and 'RRab' in DR3. The RR Lyr types given by Crestani et al. for CN Lyr ('RRc') and RW TrA ('RRab') are also inconsistent with those given in the *Gaia* catalogues ('RRab' and 'RRc', respectively). Finally, the low pulsation amplitude ($A_V \sim 0.4$ mag) for the metal-rich star FW Lup, classified 'RRab' by Crestani et al., locates it among the RRc stars in the period–amplitude diagram. More comments on these seven stars are given in Appendix A.

In the absence of high-precision photometry, or where the number and spacing of the photometry is inadequate, cRRd stars are likely to be misclassified as 'RRc', or sometimes 'RRab'. For example, only 10 per cent of the *K2* cRRd stars in the *Gaia* DR3 catalogue were correctly classified as 'RRd', while 84 per cent were misclassified 'RRc' and 6 per cent were misclassified 'RRab' (see column 5 of Table 8). Misclassification affects the photometric estimation of metallicity, $[Fe/H]_{phot}$, since the calibration equations are different for RRab, RRc, and RRd stars. To investigate the effect of misclassification $[Fe/H]_{phot}$ was calculated for the *K2* cRRd stars assuming first an 'RRc' misclassification and then an 'RRab' misclassification. In the RRc case, first-overtone period and ϕ_{31} (Table 4) were substituted into equation (3) of Nemec et al. (2013), and in the RRab case, the fundamental mode values (Table 5) were substituted into equation (4) of the same paper. The resulting difference between $[Fe/H]_{phot}$ based on the wrong type (RRc or RRab) and the correct $[Fe/H]_{phot}$ value (column 9 of Table 8) is plotted in the top panel of Fig. 12(b) (right panel). A similar graph is plotted in the lower panel for the *Gaia* stars in Table 9 that were misclassified in DR2 or DR3 and for which $[Fe/H]_{phot}$ (calculated using the same Nemec et al. calibrations – see Section 5.1 of Clementini et al. 2023) is given in the respective *Gaia* catalogue. The error due to misclassification, $\Delta[Fe/H]_{phot}$, is the difference between the *Gaia* estimate and that given in Table 9. In general, misclassifying a cRRd star as 'RRab' leads to systematic overestimation of [Fe/H] while misclassification as 'RRc' leads to systematic underestimation. Fig. 12(b) also shows that the bias is more serious in the case of RRab stars than in the case of RRc stars, and tends to increase with decreasing metal abundance (increasing period).

5 SUMMARY

Seventy-five double-mode RR Lyrae (RRd) stars observed by the *Kepler* space telescope during NASA's *K2* Mission have been identified and studied. Seventy-two of the stars are 'classical' RRd (cRRd) stars with period ratios $P_1/P_0 \sim 0.745$, and, in most cases, amplitude ratios $A_1/A_0 > 1$; none of the cRRd stars shows evidence of Blazhko amplitude or phase modulations. The other three stars are 'anomalous' RRd (aRRd) stars.

High precision periods, amplitudes, and Fourier parameters were derived for the 72 cRRd stars. Within- and between-mode correlations among the periods, amplitudes, and four low-order Fourier parameters (R_{21}, R_{31}, ϕ_{21}, and ϕ_{31}) were analysed. The results show that the within-mode period-amplitude relationships differ significantly for the two pulsation modes (see Fig. 6). The first-overtone *Kp*-amplitude tends to be around 175 mmag and decreases slightly with period, while the fundamental-mode amplitude, which is almost always lower, decreases more rapidly. Comparison with OGLE data found a similar result for the period range where the two samples overlap. These findings are consistent with the observed increase in A_1/A_0 with increasing period (seen in Fig. 2). The within-mode dependencies of the Fourier parameters on period were also investigated and compared for the two pulsation modes. Both R_{21} and R_{31} show a significant positive correlation with period for the first overtone but not for the fundamental mode (see Fig. 7). Neither ϕ_{21} nor ϕ_{31} shows a clear dependence on period for either pulsation mode (see Fig. 8).

Three cross-mode correlations and their relationships to [Fe/H] are of particular interest: P_1 versus P_0, A_1 versus A_0, and $R_{21,1}$ versus $R_{21,0}$. The P_1–P_0 diagram [see fig. 15(a) of NM21] and Petersen diagram (see Fig. 10c) were modelled by relating the two periods to [Fe/H]. An [Fe/H] calibration equation was derived from the same model. In the A_1–A_0 plane (see Fig. 9a) most of the *K2* cRRd stars have $A_1 \sim 175$ mmag regardless of the A_0 value, with a smaller fraction of the stars having lower A_1 amplitudes, and a few with higher amplitudes. The same pattern was found in OGLE data [see fig. 5(b) of NM21]. The $R_{21,1}$ and $R_{21,0}$ parameters show a different pattern of correlation: when the stars are sorted into three period classes a stratified linear relationship emerges (see Fig. 9c). For all three period classes $R_{21,1}$ increases linearly with $R_{21,0}$, with approximately constant slopes and offsets that depend on period. Since [Fe/H] depends on period the $R_{21,1}$–$R_{21,0}$ diagram might be used in conjunction with period for metal abundance estimation of cRRd stars. No separation of the three period classes was evident in the A_1–A_0 plane.

A sample of 268 cRRd stars with known spectroscopic metal abundances (see Fig. 10) was used to derive P_0–[Fe/H] and P_1–[Fe/H] calibration equations for cRRd stars (equation 6). The P_0 version of these was used to estimate metallicities for the full sample of 72 *K2* cRRd stars (Table 8) and for 2130 cRRd stars in the *Gaia* DR2 and DR3 catalogues (Fig. 11 and Table 9). Forty-nine of the 72 *K2* cRRd stars are in the Gaia DR3 catalogue. Of these, 84 per cent are misclassified 'RRc', 6 per cent are misclassified 'RRab', and only 10 per cent are correctly classified 'RRd'. The resulting metallicity bias when the wrong calibration curve is used (see Fig. 12b) was found to be more serious when cRRd stars were misclassified 'RRab' than when they were misclassified 'RRc', with the error tending to increase with decreasing metal abundance (i.e. increasing period).

ACKNOWLEDGEMENTS

Funding for the *Kepler*/*K2* Mission was provided by the NASA Science Mission directorate. JMN thanks International Statistics & Research Corporation and the Camosun College Faculty Association for supporting his travel to various *Kepler* conferences. He acknowledges interesting discussions with Radosław Poleski, Johanna Jurcsik, and Geza Kovács. The research was also supported by the 'SeismoLab' KKP-137523 Élvonal grant of the Hungarian Research, Development and Innovation Office (NKFIH).

DATA AVAILABILITY

The data underlying this article are available from the MAST website, at https://archive.stsci.edu/k2/, and all the data sets were derived from sources in the public domain.

REFERENCES

Alcock C. et al., 1997, ApJ, 482, 89
Alcock C. et al., 2000, ApJ, 542, 257
Alcock C. et al., 2004, AJ, 127, 334
Arp H. C., 1955, AJ, 60, 317
Asplund M., Amarsi A. M., Grevesse N., 2021, A&A, 653, A141
Benkő J. M. et al., 2010, MNRAS, 409, 1585
Benkő J. M., Plachy E., Szabó R., Molnár L., Kolláth Z., 2014, ApJS, 213, 31
Bingham E. A., Cacciari C., Dickens R. J., Fusi Pecci F., 1984, MNRAS, 209, 765
Bono G., Caputo F., Castellani V., Marconi M., 1996, ApJ, 471, L33
Braga V. F. et al., 2022, MNRAS, 517, 5368
Brocato E., Castellani V., Ripepi V., 1994, AJ, 107, 622
Carretta E. et al., 2009, A&A, 508, 695(C09)
Chadid M. et al., 2010, A&A, 510, A39
Chen X. et al., 2023, Nat. Astron., 7, 1081
Christy R., 1966, ApJ, 144, 108
Clement C. M., Ferance S., Simon N. R., 1993, ApJ, 412, 183
Clement C. M., Nemec J. M., 1990, J. R. Astron. Soc. Canada, 84, 434
Clement C. M., Nemec J. M., Robert N., Wells T., Dickens R. J., Bingham E. A., 1986, AJ, 92, 825
Clementini G. et al., 2019, A&A, 622, A60
Clementini G. et al., 2023, A&A, 674, A18
Coppola G. et al., 2015, ApJ, 814, 71
Corwin T. M. et al., 2008, AJ, 135, 1459
Cox A. N., King D. S., Hodson S. W., 1980, ApJ, 236, 219
Cox A. N., Hodson S. W., Clancy S. P., 1983, ApJ, 266, 94
Crestani J. et al., 2021a, ApJ, 908, 20
Crestani J. et al., 2021b, ApJ, 914, 10
Cseresnjes P., 2001, A&A, 375, 909
Di Criscienzo M. et al., 2011, AJ, 141, 81

Drake A. J. et al., 2009, ApJ, 696, 870
Drake A. J. et al., 2017, MNRAS, 469, 3688
Gruberbauer M. et al., 2007, MNRAS, 379, 1498
Hartman J. D., Bakos G. Á., 2016, Astron. Comp., 17, 1
Hatzidimitriou D. et al., 1999, AJ, 117, 3059
Hogg R. V., Craig A. T., 1959, Introduction to Mathematical Statistics. The MacMillan Company, New York, p. 219
Howell S. B. et al., 2014, PASP, 126, 398
Huber D. et al., 2016, ApJS, 224, 2
Iglesias C. A., Rogers F. J., 1991, ApJ, 371, 408
Iglesias C. A., Rogers F. J., 1996, ApJ, 464, 943
Jerzykiewicz M., Wenzel W., 1977, Acta Astron., 27, 35
Jurcsik J. et al., 2015, ApJS, 219, 25
Jurcsik J et al.. ., 2017, MNRAS, 468, 1317
Jurcsik J., Hajdu G., Dékány I., Nuspl J., Catelan M., Grebel E. K., 2018, MNRAS, 475, 4208
Kains N. et al., 2015a, A&A, 578, A128
Kains N. et al., 2015b, A&A, 582, A119
Kolenberg K. et al., 2010, ApJ, 713, L198
Kovács G., 2001, A&A, 375, 469
Kovács G., 2005, A&A, 438, 227
Kovács G., Jurcsik J., 1996, ApJ, 466, L17
Kovács G., Karamiqucham B., 2021, A&A, 653, A61
Kuehn C. A. et al., 2013, AJ, 145, 160
Kunder A. et al., 2011, AJ, 141, 15
Kunder A. et al., 2019, ApJ, 877, L17
Kurtz D. W., Bowman D. M., Ebo S. J., Moskalik P., Handberg R., Lund M. N., 2016, MNRAS, 455, 1237
Lee Y. S. et al., 2008a, AJ, 136, 2022
Lee Y. S. et al., 2008b, AJ, 136, 2050
Lenz P., Breger M., 2005, Commun. Astroseismol., 146, 53
Lomb N. R., 1976, Ap&SS, 39, 447
Lund M. N., Handberg R., Davies G. R., Chaplin W. J., Jones C. D., 2015, ApJ, 806, 30
Marconi, M. et al. . (2015) ApJ. 808:50
Molnár L. et al., 2015, MNRAS, 452, 4283
Molnár L. et al., 2018, A&A, 620, A127
Molnár L. et al., 2022, ApJSS, 258, 8
Morgan S. M., Wahl J. N., Wieckhorst R. M., 2007, MNRAS, 374, 1421
Morrison D. F., 1976, Multivariate Statistical Methods. McGraw Hill Book Company, New York, p. 302
Moskalik P. et al., 2015, MNRAS, 447, 2348
Moskalik P., Nemec J. M., Molnár L., Plachy E., Szabó R., Kolenberg K., 2018a, Proc. Polish Astron. Soc., 6, 162
Moskalik P., Nemec J. M., Molnár L., Plachy E., Szabó R., Kolenberg K., 2018b, in Ballot J., Vauclairs S., Vauclair G., eds, Proc. PHOST Conf. Geneva, Available at: https://zenodo.org/record/2204575#.YBrs8-hKiUk
Nemec J. M. et al., 2011, MNRAS, 417, 1022
Nemec J. M. et al., 2013, ApJ, 773, 181
Nemec J. M., 1985a, AJ, 90, 204
Nemec J. M., 1985b, AJ, 90, 240
Nemec J. M., Clement C. M., 1989, AJ, 98, 860
Nemec J. M., Moskalik P., 2021, MNRAS, 507, 781 (NM21)
Nemec J. M., Walker A., Jeon Y.-B., 2009, AJ, 138, 1310
Netzel H., Molnár L., Joyce M., 2023, MNRAS, 525, 5378
Netzel H., Smolec R., 2022, MNRAS, 515, 3439
Oosterhoff P. Th., 1939, Observatory, 62, 104
Petersen J. O., 1973, A&A, 27, 89
Plachy E. et al., 2016, Comm. Konkoly Obs., 105, 19
Plachy E. et al., 2017, Eur. Phys. J. Web of Conf., 160, 04010
Plachy E. et al., 2019, ApJS, 244, 32
Popielski B. L., Dziembowski W. A., Cassisi S., 2000, Acta Astron., 50, 491
Poretti E. et al., 2010, A&A, 520, A108
Preston G. W., 1959, ApJ, 130, 507
Prudil Z., Smolec R., Skarka M., Netzel H., 2017, MNRAS, 465, 4074
Sandage A., 2004, AJ, 128, 858
Sandage A., Katem B., Sandage M., 1981, ApJS, 46, 41
SAS Institute Inc., 2014, Cary. NC, USA
Scargle J. D., 1982, ApJ, 263, 835
Seaton M. J., 1994, in Nemec J. M., Matthews J. M., eds, IAU Colloq. 139. Cambridge Univ. Press, Cambridge, p. 231
Simon N. R., 1982, ApJ, 260, L87
Simon N. R., 1990, ApJ, 360, 119
Simon N. R., Cox A. N., 1991, ApJ, 376, 717
Simon N. R., Lee A. S., 1981, ApJ, 248, 291
Smolec R. et al., 2015a, MNRAS, 447, 3756
Smolec R. et al., 2015b, MNRAS, 447, 3873
Smolec R., Moskalik P., Kałużny J., Pych W., Różyczka M. , Thompson I. B., 2017a, MNRAS, 467, 2349
Smolec R., Dziembowski W., Moskalik P., Netzel H., Prudil Z., Skarka M., Soszyński I., 2017b, Eur. Phys. J. Web of Conf., 152, 06003
Smolec R., Prudil Z., Skarka M., Bąkowska K., 2016, MNRAS, 461, 2934
Sneden C. et al., 2018, AJ, 155, 45
Soszyński I. et al., 2009, Acta Astron., 59, 1
Soszyński I. et al., 2010, Acta Astron., 60, 165
Soszyński I. et al., 2011, Acta Astron., 61, 1
Soszyński I. et al., 2014a, Acta Astron., 64, 1
Soszyński I. et al., 2014b, Acta Astron., 64, 177
Soszyński I. et al., 2016a, Acta Astron., 66, 131
Soszyński I. et al., 2016b, MNRAS, 463, 1332
Soszyński I. et al., 2017a, Acta Astron., 67, 103
Soszyński I. et al., 2017b, Acta Astron., 67, 297
Soszyński I. et al., 2019, Acta Astron., 69, 321
Stellingwerf R. F., 1978, ApJ, 224, 953
Stellingwerf R. F., 2011, Carnegie Obs. Astrophys. Ser., 5, 47
Still M., Barclay T., 2012, Astrophysics Source Code Library, record ascl:1208.4
Szabó R. et al., 2010, MNRAS, 409, 1244
Szabó R. et al., 2017, Eur. Phys. J. Web Conf., 152, 02006
VandenBerg D. A. et al., 2000, ApJ, 532, 430
VandenBerg D. A. et al., 2006, ApJSS, 162, 375
VandenBerg D. A., Denissenkov P. A., 2018, ApJ, 862, 72
VanderPlas J. T., 2018, ApJS, 236, 16
Walker A. R., 1994, AJ, 108, 555
Walker A. R., Nemec J. M., 1996, AJ, 112, 2026
Zechmeister M., Kurster M., 2009, A&A, 496, 577

SUPPORTING INFORMATION

Supplementary files available at *MNRAS* online:

Appendix A. Notes on Individual Stars.

Appendix B. Fitted light curves for the RRd stars observed during *K2* Campaigns 7–18 (Figs B1–B10).

EPIC205209951_animation.gif - Animation showing the light variations of both modes of the aRRd star EPIC 205209951 (see Figs A1–A3 in Appendix A).

Table 9. Metallicities and masses for 2130 *Gaia* stars.
Table 10. Ninety-three *Gaia* 'RRd stars' with different DR2 and DR3 identification numbers.

Please note: Oxford University Press is not responsible for the content or functionality of any supporting materials supplied by the authors. Any queries (other than missing material) should be directed to the corresponding author for the article.

This paper has been typeset from a TEX/LATEX file prepared by the author.